SURFACE PASSIVATION OF NICKEL CHROMIUM ALLOYS AT ROOM TEMPERATURE

By

SHIN-FUU JENG

A DISSERTATION PRESENTED TO THE GRADUATE SCHOOL
OF THE UNIVERSITY OF FLORIDA IN PARTIAL FULFILLMENT
OF THE REQUIREMENTS FOR THE DEGREE OF
DOCTOR OF PHILOSOPHY

UNIVERSITY OF FLORIDA

1988

Rust never sleeps

Song by Neil Young & Crazy Horse

ACKNOWLEDGEMENTS

I am particularly grateful to Professor Paul B. Holloway, my advisor, for his invaluable help and guidance in this work. I would like to acknowledge Professor G. B. Hoflund for providing the author the opportunity to use his Ion Scattering Spectroscopy (ISS) equipment and D. Asbury for performing the ISS analyses. Special thanks also go to Professors C. D. Batich, R. T. McGoff and E. D. Whitney for acting on the supervisory committee. I would also like to acknowledge Dr. S. Hofmann of the Max-Planck-Institute and Dr. T. E. Madey of the National Bureau of Standards for critical discussions. I would like to thank E. Lambers and T. G. Bussing for technical assistance. The permissions of the American Institute of Physics and the John Wiley & Sons, Ltd. to reproduce Figure 5-2 and Figure 6-8(a) in this dissertation are also appreciated. Finally, I would like to express my appreciation to my wife, whose constant support and encouragement always back me up during the hard times.

TABLE OF CONTENTS

PAGE

ACKNOWLEDGEMENTS..iii

LIST OF TABLE vii

LIST OF FIGURES viii

ABSTRACT xii

CHAPTER

1 INTRODUCTION. 1

2 EXPERIMENTAL PROCEDURE 5

Sample Preparation 5
Polycrystalline Samples 5
Single Crystal Samples 6
Ultra High Vacuum (UHV) System. 9
Experimental Set-Up. 9
Oxygen Admission 10
Purity of Admitted Oxygen Gas 10
Comparison of the Gas Composition of Different Systems 15
X-ray Photoelectron Spectroscopy (XPS) 18
Ion Scattering Spectroscopy (ISS) 19
Auger Electron Spectroscopy (AES) and Electron Stimulated
Ion Desorption (ESD) 27
Auger Electron Spectroscopy (AES) 27
Electron Stimulated Ion Desorption (ESID) 27

3 SURFACE COMPOSITION OF NiCr ALLOYS. 31

Equilibrium Surface Segregation 31
Results 31
Discussion 37
Compositional Changes Induced by Ion Bombardment 45
Results 45
Discussion 45
Summary 59

4 KINETICS OF OXYGEN UPTAKE 60

PAGE

Results and Discussion ... 60
Adsorption of Oxygen ... 60
Ni(2p) and Cr(2p) spectra ... 63
Summary ... 71

5 ASSIGNMENTS OF XPS O(1s) CORE LEVEL SPECTRA ... 73

Introduction ... 73
Results ... 73
Discussion ... 76
Assignments of High Binding Energy O(1s) Peak ... 76
Identification of O(1s) Spectra by Multi-technique Analysis ... 80
Thermodynamic Basis for the Assignments of O(1s) Spectra ... 82
Summary ... 83

6 IDENTIFICATION OF MIXED REACTION PRODUCTS OF Ni ... 84

Introduction ... 84
Results ... 85
Discussion ... 89
Reaction Products on Pure Ni ... 89
A. 300 L + air-exposure ... 89
B. 300 L ... 97
Reaction Products on NiCr Alloy ... 98
Summary ... 99

7 ION SCATTERING SPECTROSCOPY OF NiCr ALLOY ... 100

Results and Discussion ... 100
Components on the NiCr Surface ... 100
Annealing Experiments ... 104
Summary ... 108

8 STRUCTURE OF OXIDE LAYER ... 110

Results ... 110
Two Layer Model ... 115
Segregation of Cr ... 125
Comparison with Previous Results ... 130
Summary ... 131

9 ELECTRON STIMULATED ION DESORPTION ... 136

Results ... 136
Desorption of O^+ ... 141
Desorption of H^+ and OH^+ ... 144
Model for Desorption of H^+ and OH^+ ... 144

PAGE

A. Desorption of OH^+ 144
B. Desorption of H^+ 145
In-situ Measurement of H^+ and OH^+ 146
Arrangements of (OH) on Ni and NiCr Surfaces 147
Summary 149

10 FORMATION OF (OH) SPECIES 150

Introduction 150
Sources for the Formation of (OH) 151
Results 151
Discussion 152
A. UHV Hydrogen 152
B. Water 158
C. Subsurface Hydrogen 160
D. Implanted Hydrogen 161
Crystal Orientation Effects 163
Thermodynamic Factors for (OH) Formation 163
Results 163
Discussion 164
Calculation of Enthalpy Changes 164
Adsorbed (OH) vs. Hydroxide 172
Results 172
Discussion 175
A. Pure Ni 175
1. 300 L 175
2. Air-exposure 176
B. NiCr Alloy 178
Summary 179

11 CONCLUSIONS 181

BIBLIOGRAPHY 184

BIBLIOGRAPHICAL SKETCH 192

LIST OF TABLES

TABLE		PAGE
2-1	Gas Composition During Leaking in Oxygen	15
2-2	Gas Composition of Different Systems	17
3-1	Parameters Used in Equation [3-1]	42
3-2	Atomic Radii and Volumes, Surface Energies and Energy of Mixing for the Ni-Cr System	43
3-3	Atomic Radii and Volumes, Surface Energies and Energy of Mixing for the Fe-Zr System	44
3-4	Heats of Segregation for Ni-Cr and Other Systems	57
4-1	Heats of Oxygen Adsorption and Formation of Oxide for Ni and Cr at 300°K	72
10-1	Enthalpy Changes for Reactions [10-1] and [10-3] to [10-6]	171
10-2	Components of Atmospheric Air	177

LIST OF FIGURES

FIGURE		PAGE
2-1	Phase diagram for NiCr alloys	7
2-2	Mass spectra obtained at (a) base pressure = 2×10^{-10} Torr before oxygen adsorption (b) $P_{O_2} = 1.5 \times 10^{-8}$ Torr and (c) $P_{O_2} = 1 \times 10^{-7}$ Torr	13
2-3	General geometry for an angle-resolved photoemission experiment. Specimen rotation for angle-resolved XPS occurred around axis θ_{hv}	21
2-4	Ag $3d_{5/2}$ peak area versus take-off angle	23
2-5	Schematic diagram of the ISS experiment	26
2-6	Electron stimulated desorption system (a) consisting of an electron gun and a quadrupole filter for mass analysis, (b) schematic of 3M prefilter for selecting the polarity and the energy of the desorbed ions	30
3-1	The ratios of Cr(38 eV) to Ni(61 eV) Auger peak-to-peak height as function of temperature	34
3-2	Arrhenius plot of calculated first layer Cr to Ni composition ratio for Ni-15%Cr(110)	36
3-3	A plot of surface tension ratio versus atomic size ratio showing that Ni (for the NiCr system) and Fe (for the ZrFe system) segregation is expected if solid surface tension per atom ratio is used- but that Cr and Zr segregation is expected when the surface tension ratio free liquids is used. The area inside (outside) the bond breaking + non-linear elasticity envelope denote expected solvent (solute) enrichment at surface.	40
3-4	The ratios of Cr(38 eV) to Ni(61 eV) Auger peak-to-peak height as function of sputtering time at room and elevated temperatures	47

FIGURE		PAGE
3-5	The Cr to Ni peak area ratios of NiCr sputtered at room temperature versus take-off angle and the least squares curve-fit data, where $R(\theta) = I_{Cr}/I_{Ni}$	53
3-6	The derived composition profile form Fig 3-5, where $C_{Cr} = n_{Cr}/(n_{Cr} + n_{Ni})$ and x/Ω = relative depth with respect to the escape depth of photoelectron	55
4-1	XPS O(1s) peak areas versus oxygen exposure for polycrystalline pure Ni, pure Cr and NiCr alloy at room temperature.	62
4-2	XPS Ni(2p) spectra as a function of oxygen exposure at room temperature for polycrystalline (a) pure Ni and (b) NiCr surface.	65
4-3	XPS Cr(2p) spectra as a function of oxygen exposure at room temperature for polycrystalline (a) pure Cr and (b) NiCr surface	69
5-1	XPS O(1s) spectra of Ni(110) surface as a function of oxygen exposure at room temperature	75
5-2	Compilation of O(1s) and Ni($2p_{1/2}$) XPS spectra for Ni(100), various Ni oxides and Ni(100) after various oxygen exposures. For the Ni(100) + O_2 spectra the intensity scales are as marked. For the oxides the scales are arbitrary.	75
6-1	Ni(2p) XPS spectra at $\theta = 45°$ for (a) Ni(110) exposed to 300 L at $P_{O2} = 5 \times 10^{-8}$ Torr (b) Ni(110) exposed to air for 5 minutes subsequent to (a) (c) polycrystalline NiCr alloy exposed to 300 L at $P_{O2} = 5 \times 10^{-8}$ Torr (d) polycrystalline NiCr alloy exposed to air for 5 minutes subsequent to (c).	88
6-2	The difference Ni(2p) XPS spectra after subtraction of background and metallic Ni spectra, (a) Ni(110) exposed to 300 L O_2 + air, (b) Ni(110) exposed to 300 L O_2, (c) NiCr alloy exposed to 300 L O_2 + air; (d) NiCr alloy exposed to 300 L O_2.	91

FIGURE		PAGE
6-3	O(1s) XPS spectra versus take-off angle for Ni(110) exposed to 300 L at 5 x 10^{-9} Torr	96
7-1	1 keV He^+ ISS spectra taken from pure Ni, pure Cr, clean NiCr alloy and oxidized NiCr alloy (100 L O_2 at room temperature)	102
7-2	1 keV ISS spectra as a function of heating time at 500°C for NiCr alloy exposed to 100 L O_2 and 1 keV ISS spectrum of clean NiCr alloy	105
7-3	Auger peak to peak or peak to background intensities versus heating time at 500°C in vacuum	107
8-1	Ni(2p), Cr(2p) and O(1s) XPS spectra versus take-off angle for NiCr alloy exposed to 300 L O_2.	112
8-2	The peak area ratios of Cr oxide to Ni hydroxide and Cr metal to Ni metal versus take-off angle for NiCr alloy exposed to 300 L O_2	114
8-3	Ni(2p) and Cr(2p) XPS spectra of an oxidized (300 L) NiCr alloy after sputtered by 4 keV, 1.5 μA Ar^+ for 1 minute.	117
8-4	A two-layer model for oxide formed on NiCr alloy after 300 L O_2 exposure	119
8-5	Experimental A(θ) (see text) versus take-off angle. The dashed lines are calculated based on equation 8-6 in the text where t_1 = 1 ML	124
8-6	Cr(2p) XPS spectra at θ = 45° for NiCr alloy and pure Cr exposed to 300 L O_2.	129
8-7	Schematic of the model derived from angle-resolved XPS analysis for the surface of NiCr alloy exposed to 100 L O_2 at room temperature	133
8-8	Sequential sputter model, (a) Auger peak intensities versus sputter time for Ni-20%Cr alloy exposed to 400 L O_2 at room temperature, (b) Quantitative analysis of the sputter profile shown in Fig. 8-8(a)	135
9-1	ESD mass spectra for (a) Ni(110) and (b) NiCr(110) exposed to 300 L O_2 at room temperature	138

FIGURE		PAGE
9-2	ESD H⁺ and OH⁺ intensities and XPS OH O(1s) peak area versus oxygen exposure for (a) Ni(110); (b) NiCr(110)	140
10-1	O(1s) spectra at θ = 15° for Ni(110) (a) exposed to 300 L O_2 at P_{O2} = 5 x 10^{-8} Torr and (b) exposed to 300 L (O_2 + H_2O) at $P_{O2} = P_{H_2O}$ = 5 x 10^{-8} Torr	154
10-2	O(1s) XPS spectra at θ = 45° for (a) sputtered unannealed and (b) well annealed Ni(110) both exposed to 300 L O_2 at 5 x 10^{-8} Torr	156
10-3	O(1s) spectra at θ = 45° for polycrystalline pure Ni, pure Cr and NiCr alloy exposed to 300 L O_2	166
10-4	Enthalpy changes which accompany adsorption and dissociation of water referenced to gas phase molecular hydrogen and oxygen	168
10-5	O(1s) and Ni(2p) XPS spectra at θ = 15° for Ni(110) exposed to (a) air for 5 minutes and (b) 300 L O_2	174

Abstract of Dissertation Presented to the Graduate School of the University of Florida in Partial Fulfillment of the Requirements for the Degree of Doctor of Philosophy

SURFACE PASSIVATION OF NICKEL-CHROMIUM ALLOYS AT ROOM TEMPERATURE

By

Shin-Puu Jeng

April, 1978

Chairman: Professor Paul H. Holloway
Major Department: Materials Science and Engineering

The surface composition and room temperature oxidation of atomically clean single crystal Ni-15%Cr(110) and polycrystalline Ni-23%Cr alloy have been studied using Auger Electron Spectroscopy (AES), X-ray Photoelectron Spectroscopy (XPS), Ion Scattering Spectroscopy (ISS) and Electron Stimulated Ion Desorption (ESID). It was found that Ni segregated preferentially to the surface of Ni-15%Cr(110) in vacuum at temperatures between 500 to 650°C, and the heat of segregation was 2550 cal/mole. The subsurface region of the Ni-Cr alloy was depleted in Ni during Ar ion bombardment at temperature above 200°C, which is in agreement with the model of preferential sputtering of Ni caused by radiation-enhanced surface segregation of Ni. But the subsurface region of room temperature

sputtered Ni-Cr alloy was depleted in Cr. Possible causes for this observation were discussed.

During oxidation of NiCr alloys, the Cr was quickly converted to oxide after 1 to 2 L of oxygen exposure. Reaction of Ni with oxygen occurred more slowly than the Cr/O_2 reaction, but much more rapidly than for pure Ni. The oxides coalesced and completely covered the surface at 30 L of oxygen exposure. Quantitative angle-resolved XPS data suggested that the room temperature passivating oxide on the alloy had two layers. The outer oxide (one monolayer thick) was a mixture of Ni hydroxide and Cr oxide, and the inner oxide (four monolayers thick) consisted of Cr_2O_3, small amounts of NiO and possibly metallic Ni. In addition, a layer having extra metallic Ni existed in the subsurface region next to the oxide layer. Both pure Cr and Cr in the alloy had the same oxidation reaction product, Cr_2O_3. In contrast, the major reaction product of nickel in alloy was Ni hydroxide, while that of pure Ni was NiO. Apart from NiO, adsorbed hydroxyl species was found on the oxidized Ni surface. Formation of hydroxyl species under normal UHV oxygen was discussed, with the conclusion that impurity hydrogen in UHV system was the major cause. Formation of Ni hydroxide was limited to the first monolayer, clearly demonstrating that alloying dramatically modified the oxidation behavior.

CHAPTER 1
INTRODUCTION

Metals are inherently thermodynamically unstable and will react with atmospheric gases generally producing oxides, hydrated oxides or hydroxides. Normally these products will degrade the mechanical and physical properties of the metallic parts. Fortunately the oxides produced by the reactions usually reduce the rate of subsequent reaction making it feasible to build structures with metals.

For convenience, the process of oxidation can be divided into two regimes: high temperature and low temperature (1). When the product of the oxidation reaction is solid, it separates the two reactants --gas and metal-- so that continuation of the reaction requires a species of metal and/or oxygen to dissolve in and move through the growing oxide. Barriers to ion (or atom) movement into and through the oxide exist. The means for overcoming these barriers form the basis for distinguishing low- and high-temperature oxidation. In high-temperature oxidation, thermal energy is sufficient to allow the ion (or atom) movement through the oxide. A parabolic rate law is generally followed. In low-temperature oxidation where the thermal energy is insufficient to allow existing ions (or atoms) to surmount the energy barrier, an alternative driving force such as electrical fields or stress has been postulated to account for the continued logarithmic reaction rate (2).

The oxide films formed at temperatures below 250°C are very thin (usually ≤ 30 Å). Despite their thinness, they are very important for many practical situations. Apart from protection of metals from being corroded, the thin stable oxides formed by oxidation at room temperature play important roles in promoting lubrication between two metal surfaces (3), in adhesion of nonmetals to metals (4) and in diffusion of gases out of metals (5). Oxidation at low temperatures is increasingly important in electronic components such as contacts and integrated circuits. An increase in contact resistance due to oxidation is a problem in integrated circuits, but thin oxide films also play a key role in the proper functioning of solid state devices (6-8). For example, the thermal oxidation of silicon to passivate its surface is a crucial step in semiconductor device technology. Moreover, thin oxide films are also parts of both passive and active solid state devices (9). An example of the former is tantalum oxide capacitors. Examples of the latter include tunneling junctions and MOS transistors etc.

Though oxidation of metal at room temperature has both fundamental and practical importance, it has received little attention compared to the high temperature oxidation. This is particularly true for alloys which have more complicated oxidation mechanisms than pure metals. Generally, the properties of binary alloys cannot be regarded as an additive combination of the corresponding characteristics of the pure constituents. The surface composition of an alloy may differ markedly from the bulk due to

surface segregation of one component. Concerning the reaction with oxygen, selective oxidation of one alloy component may occur, even if both pure metals may form stable oxides. Furthermore, the reaction products of an alloy can be different from that of pure metals as a result of alloying.

Alloys of NiCr are often used in high temperature oxidizing environments (10). In addition to their high temperature applications, NiCr thin films are also widely used as conductive materials in small resistors and potentiometers because of their extremely small temperature coefficient of resistance (TCR) (11-17).

It has been found for nichrome (NiCr) alloys that addition of chromium (≥ 10%) significantly improves the ability of the oxides to passivate (reduce the reaction rate of) the metallic surfaces, yet the mechanism by which this resistance is increased is only poorly understood (10). Thus, we have studied the reaction of oxygen with atomically clean NiCr alloys at room temperature and compared them with the more thoroughly studied oxygen reactions with the pure components. Surface sensitive techniques like X-ray Photoelectron Spectroscopy (XPS), Auger Electron Spectroscopy (AES), Ion Scattering Spectroscopy (ISS) and Electron Stimulated Ion Desorption (ESID) were used in this study. These techniques allowed us to determine the chemical states of the reaction products and the composition profile of the oxide layer. In particular, ESID technique provided us the ability for detecting hydrogen and hydroxyl species at solid surfaces. It was interesting to find that the formation of Ni

hydroxide rather than Ni oxide occurred on NiCr alloy under the normal UHV oxygen exposure so the observed electron stimulated O^{+} and H^{+} desorption signals were correlated to the XPS data.

The major purpose of this work is to understand the effects of the additions of Cr on the oxidation of Ni at room temperature. Emphasis has been put on (1) determining the surface compositions of atomically clean NiCr at thermal equilibrium and during ion bombardment, (2) identifying the various reaction products formed on surfaces under different oxidizing environments, (3) modeling the complicated structure of NiCr oxide formed at room temperature and (4) studying the formation of hydroxyl species on the oxidized alloy surface.

CHAPTER 2
EXPERIMENTAL PROCEDURE

Sample Preparation

Both polycrystalline and monocrystalline Ni, Cr and NiCr samples were used in this study. For the composition of alloys used (Ni with 15% - 23% atomic Cr), the Ni-Cr binary phase diagram (see Fig. 2-1) indicates a single phase face centered cubic structure (FCC, i.e., same as for pure Ni) is present between 650 °C and room temperature (18). In the same temperature range, pure Cr exhibits a body centered cubic (BCC) structure with limited solubility for Ni.

Polycrystalline Samples

Polycrystalline Ni-23%Cr alloy was prepared from 99.99% pure Ni and Cr obtained from AD Mckay. The pure elements were weighed and degreased ultrasonically with acetone before melting. The basic method of preparation involved co-melting of the pure elements on a cold-hearth mono-arc melter which had been evacuated to 10^{-5} Torr and backfilled with high purity Ar to ~0.5 atm. A pure titanium getter was premelted in order to reduce the reactive contaminants in the chamber.

Fig. 2-1 Phase diagram for NiCr alloys.

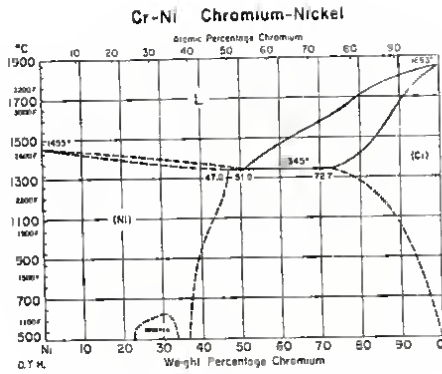
Cr-Ni Chromium-Nickel
Atomic Percentage Chromium
°C
1900
1700
1500
1300
1100
900
700
500
10
20
30
40
50
60
70
80
90
L
1455°
1345°
1453°
(Cr)
(Ni)
47.0
51.0
72.7
Ni
Cr
Weight Percentage Chromium

Slices of the alloy boules ca. 1 cm in diameter and 1 mm in thickness were cut and polished by standard metallographic techniques. The general procedure involved an initial stage using 220 grit silicon carbide paper followed by 400 grit and then 600 grit and for the final stage, electropolishing using dilute HNO_3 solution.

Reactions of pure polycrystalline Ni and Cr were also studied using the starting materials for the arc melted alloys. It is known that the crystal orientation of the metal has effects on the oxidation rate, so the crystalline textures of these polycrystalline samples were examined by using the electron channeling techniques. Though the number of grains identified was limited, no evidences for the existence of strong orientation textures in any of these polycrystalline samples was found.

After the samples were introduced to the UHV chamber, the polycrystalline samples were sputter cleaned by a differentially pumped ion gun using a rastering Ar^+ beam with an energy of 4 keV. Sputtering continued until no impurities except Ar were detected by XPS. The sputtered unannealed samples were used for oxidation experiments.

Single Crystal Samples

The Ni-15%Cr(110) and Ni(110) single crystals were obtained as high purity samples from Argonne National Laboratories and from Monocrystals Company, respectively. The orientations of the single crystals were checked by the electron channeling technique and shown

to be within ± 1° of the (110), and clean annealed samples showed a standard (110) LEED pattern.

Single crystal samples were carefully cleaned by a cyclic sputter-annealing procedure until no impurities could be detected by AES in the UHV chamber. The sample was spot welded to Pt wires and heated by a tungsten filament from the rear. To monitor the temperatures, a W-5%Re/W-26%Re thermocouple was spot welded to the back of the sample. Prior to surface segregation and oxidation experiments, single crystal samples were first sputter cleaned, then annealed at 650 °C for 30 minutes and cooled to the desired temperature.

Ultra High Vacuum (UHV) System

Experimental Set-Up

All the experiments (except ion scattering experiment) were performed in a standard bakable stainless steel UHV system from Perkin Elmer. The system is equipped with a 220 l/sec Ultek ion pump. Titanium sublimation pumping is provided with a Penstvac four-spiral filament holder mounted horizontally in the pump module. All of these facilities lie below a poppet valve that separates the pumping chamber from the bell jar. Two Ultek sorption pumps are used for roughing. The system was baked up to ~200 °C for 24 hours prior to the experiments. The residual base pressure of the chamber was better

than 2×10^{-10} Torr, and the main residual gases after baking were H_2, He, CO and Ar.

The partial pressures of admitted and background gases were measured with a Dycor Model M100M quadrupole residual gas analyzer (RGA) with tungsten filaments. In order to quantitatively analyze the partial pressures using the published ionization cross sections, the ionizer of RGA was operated at a standard potential of 70 volt. The electron multiplier was turned off during analysis and the ion currents of different gas species were directly measured by a Faraday cup.

Oxygen Admission

The oxygen gas used in this study was obtained from Matheson as research grade and has a purity of 99.99% minimum. The oxygen admission line was cleaned by repeatedly ganging and flushing with oxygen. Because residual gases reached an intolerable level ($\geq 10^{-7}$ Torr) when the ion pump was completely isolated from the UHV chamber and O_2 was getter-pumped by Ti, a steady flow of oxygen was introduced into the chamber through a leak valve with the ion pump operating. The oxygen partial pressure was maintained between 10^{-8} and 10^{-7} Torr during the oxidation experiment.

Purity of Admitted Oxygen Gas

Researchers in the field of oxidation generally use research grade oxygen in systems whose base pressures are usually in the 10^{-10}

Torr range, therefore the purity of gas is assumed to be satisfactory However, maintenance of the purity of reactive gases like hydrogen, oxygen or water vapor is known to be a serious problem for ion-pumped UHV systems (19,20,21). For example, during hydrogen exposure Sauer and Poppe (20) observed that the compositions of both H_2O and CH_4 residual gases were increased as a result of interactions with the ion pump Beerdorf and co-workers (21) also found a large increase in hydrogen pressure when water was admitted into the UHV system

In this study, research grade oxygen gas of spectroscopic purity was also significantly degraded in purity when admitted to the UHV system as shown by the RGA spectrum in Fig 2-2. The background gases found in the UHV chamber at oxygen partial of 10^{-9} and 10^{-7} Torr are similar being dominated by H_2, He, CH_4, Ne CO Ar and CO_2 while H_2O is only a minor constituent being about two order magnitude lower than O_2. As shown in Fig.2-2(b),(c) the relative amounts of gases vary with oxygen partial pressure or the flow rate of oxygen For example noble gases are the most prominent residual gases at $P_{O2} = 1 \times 10^{-7}$ Torr, while H_2 is the most abundant contaminant at $P_{O2} = 1.5 \times 10^{-9}$ Torr.

Several possible sources or processes may be responsible for the degraded purity of oxygen in the UHV chamber, such as

(a) contaminants from insufficiently baked gas inlet system,

(b) chemical reactions in the system, such as production of water from reaction of hydrogen and oxygen either on the surface of hot

Fig. 2-2 Mass spectra obtained at (a) base pressure = 2×10^{-10} Torr before oxygen admission, (b) $P_{O2} = 1.5 \times 10^{-8}$ Torr and (c) $P_{O2} = 1 \times 10^{-7}$ Torr.

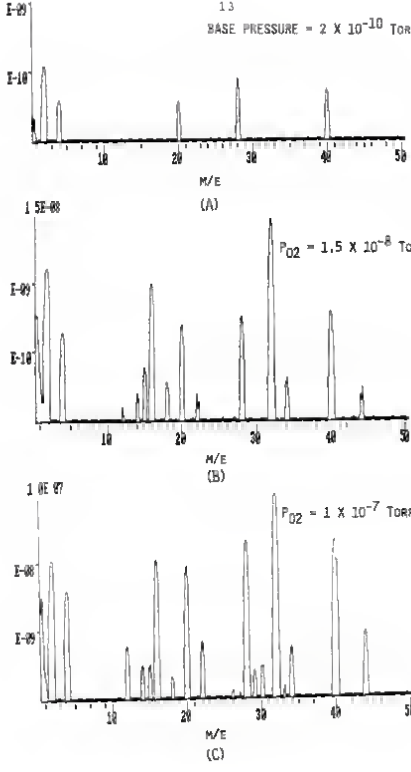
BASE PRESSURE = 2 X 10⁻¹⁰ TORR
M/E
(A)
P_O2 = 1.5 X 10⁻⁸ TORR
M/E
(B)
P_O2 = 1 X 10⁻⁷ TORR
M/E
(C)

filament or at the chamber wall,

(c) replacement desorption of some gases, which adsorbed initially on the chamber wall, are displaced by the oxygen;

(d) impurity gases produced in the ion pump at high gas load;

(e) the ion pump memory effects arising from the regurgitation of previously pumped gas.

None of the possibilities above can be entirely excluded. However, the contaminants from the oxygen admission line appear to be unlikely, since water generally is the major residual gas in an air-exposed and unbaked vacuum system and the water content is quite low in our UHV chamber during admission of oxygen. Interactions between admitted oxygen gas and ion pump are considered to be the major cause for the degradation in the present case. It has been reported that background water vapor was reduced when the admitted hydrogen pressure was maintained at constant pressure by a turbomolecular pump rather than an ion pump (20). In addition to the oxygen/ion pump interaction, contaminants which displaced from chamber wall may be another major cause for degradation.

The approximate partial pressures of different gas species in Fig. 3-2 were calculated directly from ion current with correction of ionization cross section. The relative ionization cross sections, $\sigma(J)$ were either obtained from the literature (22) or estimated from the following equation (23,24):

$$\sigma(J) = 0.6 \times (\Sigma Z/14) + 0.4 \qquad [2-1]$$

where Σ Z is the total number electrons in a molecule. The partial pressures for $P_{O_2} = 1.5 \times 10^{-8}$ Torr are shown in Table 2-1.

Table 2-1, Gas Composition During Leaking in Oxygen

$P_{O_2} = 1.5 \times 10^{-8}$ Torr

Gas	I(J)	Partial pressure (Torr)	Relative amount (%)
H_2	0.42	8.9×10^{-9}	59.2
He	0.14	2.4×10^{-9}	16.0
CH_4	1.57	1.2×10^{-9}	7.9
H_2O	0.83	8.2×10^{-11}	0.54
Ne	0.22	2.1×10^{-9}	14.0
CO	1.07	7.1×10^{-10}	4.8
O_2	1.02	1.5×10^{-8}	100.0
Ar	1.19	6.6×10^{-10}	4.4
CO_2	1.36	4.0×10^{-12}	0.27

Comparison of the Gas Compositions in Different UHV Systems

In order to learn the degree of variations of oxygen purity in different oxidation experiments, the gas composition in our UHV system is compared with some reported results (19,24) in Table 2-2.

These published results are generally obtained under well controlled experimental conditions especially for (19), but different gas compositions are reported. While error in accuracy can be attributed to the scatter in the data, the variation of oxygen purity among different systems is considered to be real.

Despite similar apparatus and starting base pressure for different systems, the gas composition of each system can be changed drastically by experimental parameters, such as the partial pressure and flow rate of oxygen gas, and the cleanliness of the gas inlet system. Other more "subtle" parameters, such as the cathode voltage, the contamination level of cathode surface, history of ion pump and the material of operating hot filament, can also have profound effects on the compositions of residual gases. As shown in Fig. 2-2, when the partial pressure of oxygen increases from 1.5×10^{-9} Torr to 1×10^{-7} Torr, noble gases (He + Ne + Ar) rather than hydrogen are the dominant residual gases.

It has been reported that water content is generally lower in the ion-pumped systems as compared to diffusion-pumped systems at a similar pressure ($\leq 10^{-10}$ Torr) (25). Due to different operating principles, interactions of admitted oxygen gas with vacuum pumps of a different type are expected to be different. Because some active residual gases, particularly hydrogen and water, are likely to participate in oxidation reactions, it is important to measure the gas composition in order to assist to the prediction of possible reaction products. Moreover, large variations in the compositions of

residual gases in different systems strongly suggest that caution should be taken when comparing oxidation data obtained under different experimental conditions and with different systems.

In summary, the admission of oxygen causes changes in residual gases in an ion-pumped UHV chamber. The amounts of residual gases vary significantly with experimental parameters such as partial pressure of oxygen. For the present case, hydrogen is the major active residual gas at $P_{O_2} = 10^{-7}$ to 10^{-8} Torr, while the partial pressure of water is lower than oxygen by two orders of magnitude.

Table 2-2, Gas Composition of Different Systems (Relative Amounts %)

	ref(19)	ref(24)	present work
P_{O_2} (Torr)=	1.25×10^{-7}	1.5×10^{-7}	1.5×10^{-8}
H_2	6.5	0.5	59.2
He+Ne+Ar	127.4	20.8	34.4
CO	30.8	3.0	4.6
O_2	100	100	100
H_2O	3.2	0.75	0.54
CO_2	1.9	0.83	0.27

X-ray Photoelectron Spectroscopy (XPS) (26,27)

The XPS data were obtained using a Perkin Elmer Model 5100 spectrometer with Mg K_α radiation from a source operated at 15 kV and 300 W. The analyzed area was 2 x 10mm and the pass energy of 37.5 eV gave a constant energy resolution, $\delta E = 0.5$ eV. Samples were mounted on a rotatable sample holder with a stepping motor which allowed automatic angle-resolved XPS data collection. The geometry for the angle-resolved photoemission experiment is shown in Fig 2-3.

The intensity of photoelectron flux from the ith orbital of an element which has a concentration over depth of the $C_i(x)$ is a function of the angle θ (28)

$$I_i(\theta) = K_i(\theta)\,\sigma_i \int_0^{t1} C_i(x)\,\exp[-x/(\Omega_i \sin\theta)]\,dx \qquad [2-2]$$

where K_i represents a combined response function of analyzer and excitation flux as a function of θ. σ_i is the photoionization cross section. Ω_i is the mean escape depth of the photoelectron and $C_i(x)$ is the depth composition functions. The exponential term represents the attenuation of flux originating at a depth of x. The take-off angle θ can be varied from 90° to less than 5° by rotating the sample holder; which provides an effective change in sampling depth ($\Omega_i \sin\theta$) of greater than a factor of 10.

Some factors, such as surface roughness and reflection and refraction of electron and x-ray can affect the results of Angle

Resolved X-ray Photoelectron Spectroscopy (ARXPS). The importance of these effects tends to increase as θ approaches a low grazing angle but reflection and refraction of electron are considered to be negligible at θ ≥ 15° (29). Forward scattering of photo-electrons from a single crystal is also known to effect the measurement of photoelectron intensities (30). However the effects are expected to be small for polycrystalline samples since the effects should be cancelled by the large number of grains of different orientations. The $Ag(3d_{5/2})$ photoelectron intensity curve as a function of take-off angle from a sputtered clean polycrystalline Ag sample is shown in fig 2.4. no forward scattering peaks are observed.

The samples were in situ Ar^+ sputter cleaned using a differentially pumped ion gun with a rastering beam incident at 45° relative to the sample surface. During the sputtering, the system pressure was held at 10^{-8} - 10^{-7} Torr.

Ion Scattering Spectroscopy (ISS) (31,32)

Ion scattering experiments were carried out using a double pass CMA (PHI model 15-255GAR) equipped with an angular resolving aperture. The ion gun (PHI model 04-161) was positioned at an angle of 63° with respect to the surface plane and a primary beam of Ne ions with an energy of 1 keV was used. Because of the geometric restrictions of the instrument, the smallest obtainable scattering angle was 63°. The sample was positioned at an angle of 45° with

Fig. 2-3 General geometry for an angle-resolved photoemission experiment. Specimen rotation for angle-resolved XPS occurred around axis θ, θ_{av}.

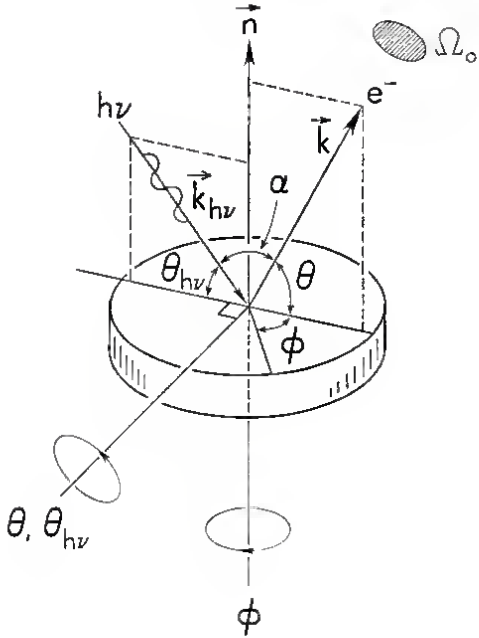
n
Ω₀
hν
e⁻
k
k_hν
α
θ_hν
θ
ϕ
θ, θ_hν
ϕ

Fig. 2-4 Ag $3d_{5/2}$ peak area versus take-off angle.

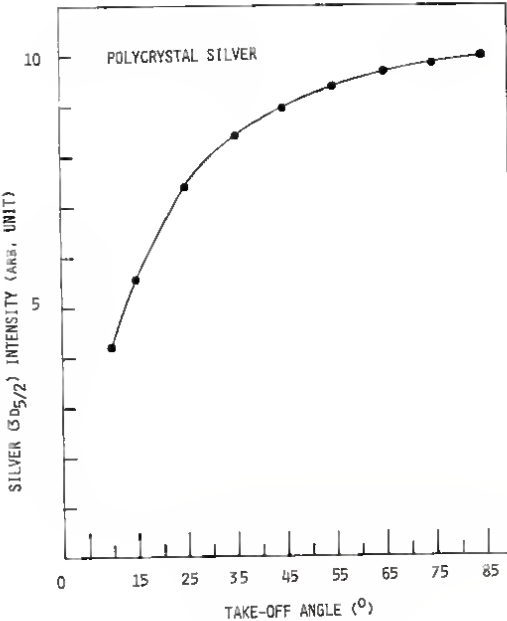
POLYCRYSTAL SILVER
10
5
SILVER ($3d_{5/2}$) INTENSITY (ARB. UNIT)
0
15
25
35
45
55
65
75
85
TAKE-OFF ANGLE (^{o})

respect to the CMA axis, and the angle resolving aperture was used to select Ne ion scattered at an angle of 13° with respect to the surface plane (Fig.2-5).

Qualitative identification of elements was done by using equation (2-2) which is based on the law of energy and momentum conservation (31,32)

$$(E_1/E_0) = \{[\cos\theta \pm (A^2 - \sin^2\theta)^{1/2}] / (1 + A)\}^2 \quad A = M_2/M_1, \qquad [2-3]$$

in which E_0 is the incident energy E_1 is the energy of the scattered ion θ is the laboratory scattering angle between incident beam and scattered beam and M_1 and M_2 are the masses of incident ion and target atom respectively. The positive sign in equation [2-3] is used for all cases where $A > 1$ (i.e, when the target atom is heavier than the incident ion) or for cases where $\theta < \sin^{-1} A$, if the target atom is lighter than the incident ion. Under the present experimental conditions the oxygen is lighter than neon and $\theta = 75°$ which is larger than the maximum critical scattering angle for observing oxygen, $\sin^{-1}(16/20) = 53.13°$. Sigle scattering from oxygen was not detectable.

Data acquisition time and the primary ion current were minimized to reduce sputtering effects (i.e operate in the static mode)

Fig. 2-5 Schematic diagram of the ISS experiment.

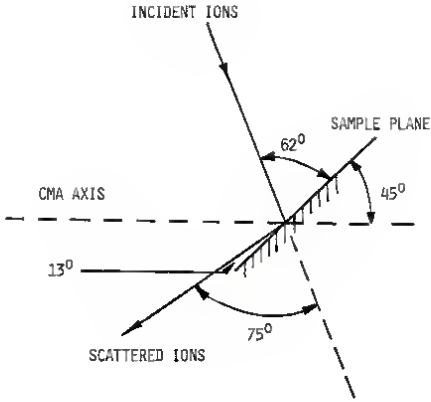
INCIDENT IONS
SAMPLE PLANE
62°
45°
CMA AXIS
13°
75°
SCATTERED IONS

Auger Electron Spectroscopy (AES) and Electron Stimulated Desorption (ESD)

Auger Electron Spectroscopy (AES) [27]

The AES experiments were performed in a Perkin Elmer/Physical Electronics Model 545 Scanning Auger Microprobe (SAM) with a base pressure of ~2 x 10^{-10} Torr. The sample was positioned at an angle of 45° with respect to the CMA axis. Data were recorded in the derivative mode using a modulation voltage of 1 eV p-p and a primary beam energy and current of 3 keV and 5 μA respectively. The spot size of the electron beam is approximately 10 μm in diameter.

Electron Stimulated Desorption (ESD) [33-35]

For ESD, a UTI quadrupole mass filter with a 3M Co. prefilter was mounted in the same SAM chamber. A rectangle 0.3 x 0.5 mm on the sample was irradiated by a 130 eV, 500 mA/cm^2 electron beam from the Auger electron gun. To improve ion collection, the distance between sample and quadrupole was minimized to ~10 cm, and the sample normal was only a few degrees off the quadrupole axis. The experimental set-up is shown in Fig. 2-5.

Sources of ions other than ESD from the sample were checked by varying the partial pressure of oxygen and hydrogen gas. It was found that both H^+ and OH^+ ion yields were not affected by the background gases like hydrogen and water, but the O^+ ion yield was significantly interfered with by gas phase oxygen. Therefore, both H^+ and OH^+ ion yields were monitored during oxygen exposure, while the entire ESD

spectra (including O^+) from the oxidized surface was taken only after oxygen was evacuated from the chamber

Fig. 2-6 Electron stimulated desorption system (a) consisting of an electron gun and a quadrupole filter for mass analysis; (b) schematic of 3M prefilter for selecting the polarity and the energy of the desorbed ions.

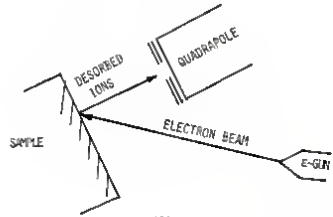
DESORBED IONS
QUADRAPOLE
SAMPLE
ELECTRON BEAM
E-GUN

(A)

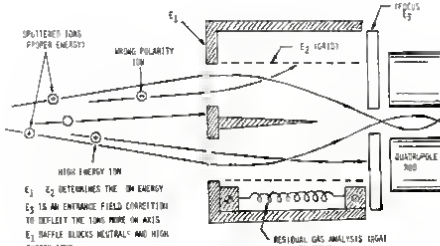
SPUTTERED IONS (PROPER ENERGY)
WRONG POLARITY ION
HIGH ENERGY ION
E_1
E_2 (GRID)
(FOCUS E_3)
QUADRUPOLE MASS
RESIDUAL GAS ANALYSIS (OR) FILAMENT
E_1 E_2 DETERMINES THE ION ENERGY
E_3 IS AN ENTRANCE FIELD CORRECTION TO DEFLECT THE IONS MORE ON AXIS
E_3 BAFFLE BLOCKS NEUTRALS AND HIGH ENERGY IONS

(B)

CHAPTER 3
SURFACE COMPOSITION OF NiCr ALLOYS

Equilibrium Surface Segregation

The surface composition of a multicomponent solid may differ from that of the bulk as a result of preferential segregation of one or more components to the surface. The extent of surface segregation observed at equilibrium during heating in a vacuum can be modified by oxidation, gas adsorption, and sputtering. For atomically clean metallic alloys, thermodynamic equilibrium surface segregation is driven mainly by the lowering of surface energy and the relief of bulk strain energy (36), but the heat of mixing of alloys can modify the extent of segregation (37).

Results

We have studied the equilibrium surface segregation of Ni-15%Cr(110) at temperatures between 500°C and 650°C. The alloy was carefully cleaned by a cyclic sputter-annealing procedure until no impurities could be detected by AES. Therefore the surface impurity concentrations, including O, S, N, and C, were estimated to be below 0.5% throughout the experiment. The AES spectra were recorded in situ during heating. The sample was first annealed at 650°C for 30 minutes in order to relax any possible composition gradient generated by ion

sputter cleaning. The sample was then cooled to the temperature of interest, and the equilibrium condition was assumed to be obtained when no further changes could be observed in the AES spectra after a minimum of 30 minutes at the new temperature. No changes in peak shape or background were observed in the experimental temperature range of 500 - 650°C. The AES peak height ratios of Cr(38 eV) and Ni(61 eV) MVV Auger transitions as a function of temperature are shown in Fig 3-1. The low energy peaks were used because of their surface sensitivities. The data show that Ni segregated preferentially to the surface as the temperature was decreased. Assuming that Ni segregation was limited to the outer monolayer, the composition of the surface monolayer can be calculated from (38)

$$\frac{I_{Cr}}{I_{Ni}} = \frac{I^{\infty}_{Cr} K_{Cr} [X^{\alpha}_{Cr} [1 - \exp(-1/Q'_{Cr})] + X^{b}_{Cr} [\exp(-1/Q'_{Cr})]}{I^{\infty}_{Ni} K_{Ni} [X^{\alpha}_{Ni} [1 - \exp(-1/Q'_{Ni})] + X^{b}_{Ni} [\exp(-1/Q'_{Ni})]} \qquad [3-1]$$

where X_i is the mole fraction of either Cr or Ni, I_i is Auger intensity from pure elemental standards, K_i is a correction factor for backscattering, and Q_i is the effective electron mean free path corrected for emission angle relative to the surface ($Q_i = Q_i \cos\theta$). Using the parameters in Table 3-1, the logarithm of surface chromium to nickel concentration ratio was calculated from data in Fig.3-1 and plotted versus inverse absolute temperature in Fig.3-2. The heat of segregation of Ni to the surface is determined to be 2.550 cal/mole

Fig. 3-1 The ratios of Cr(38 eV) to Ni(61 eV) Auger peak-to-peak height as function of temperature

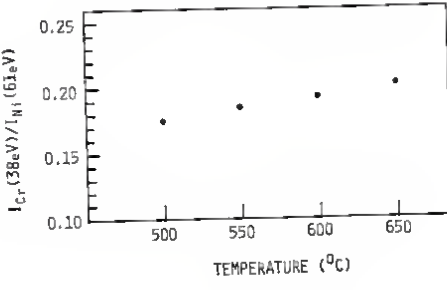
0.25
0.20
0.15
0.10
$I_{Cr}(3BeV)/I_{Ni}(6BeV)$
500
550
600
650
TEMPERATURE (^0C)

Fig. 3-2 Arrhenius plot of calculated first layer Cr to Ni composition ratio for Ni-15%Cr(110).

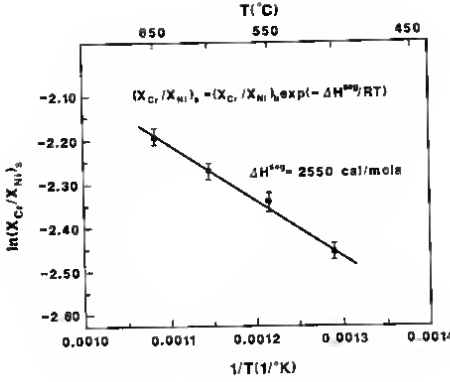
T(°C)
650
550
450
$(X_{Cr}/X_{Ni})_s = (X_{Cr}/X_{Ni})_0 \exp(-\Delta H^{seg}/RT)$
ΔH^{seg}= 2550 cal/mole
$\ln(X_{Cr}/X_{Ni})_s$
-2.10
-2.20
-2.30
-2.40
-2.50
-2.60
0.0010
0.0011
0.0012
0.0013
0.0014
1/T(1/°K)

Discussion

Since the surface impurity concentrations were below AES detection limits it seems reasonable to exclude the possibility that impurities caused Ni segregation. In fact, the crystal was intentionally contaminated with small amounts of oxygen and Cr segregated to surface rather than Ni. Segregation of Ni to atomically clean NiCr alloy surface apparently is due to the lowering of surface energy and the relief of strain energy (36). However segregation of Ni to NiCr alloy surface is still somewhat unexpected. The atomic radii of Ni and Cr are approximately equal (Cr is 3% larger) and the liquid surface tension of Cr is smaller than that of Ni (39). As a result, both size and liquid surface tension qualitatively indicate that Cr rather than Ni should segregate to the surface. By using Abrahm and Brundle's theoretical segregation model which considers both bond breaking and bulk strain energy (36) it is also expected that Cr segregates to the surface of NiCr alloy. (see Fig.3-3)) The experimental observations are obviously contrary to theory. However theoretical predictions are consistent with experiments if the surface energies of solid Cr and Ni are used instead of liquid surface tensions as shown in Fig 3-3. This reversal in predicted segregated species results from the fact that the surface energy of solid Ni is smaller than that of solid Cr, contrary to the surface tensions of liquid elements (see Table 3-2).

The difference in surface energy per unit area is only 7% lower, but this difference is sufficient to lead to a prediction in Fig 3-3

of Ni segregation. However, the basis for comparing the solid surface energy of Ni and Cr should be on a per atom rather than a per unit area basis. For substitutional binary alloys, surface segregation can be viewed as an exchange reaction at the first monolayer:

$$A^{surface} + B^{bulk} \leftrightharpoons A^{bulk} + B^{surface} \qquad [3-2]$$

The exchange process is based upon the fact that one segregating atom from the bulk displaces one atom at the surface while the surface atom density remains constant near equilibrium. A lower surface energy per unit area, Γ_{area} does not guarantee a lower surface energy per atom, Γ_{atom}. Since data on the variation of surface energy with crystal orientation are not available, we have used an averaged surface energy per atom calculated from the relation

$$\Gamma_{atom}(erg/atom) = \Gamma_{area}(erg/cm^2) \;/\; N(atom/cm^2) \qquad [3-3]$$

where the average surface atom density, N, is derived from the atomic volume, V, using the relation

$$N = (6.02 \times 10^{23} \;/\; V)^{2/3} \qquad [3-4]$$

Using the solid surface energies in Table 3-2, Γ_{atom}^{Ni} is calculated to be 0.96×10^{-12} erg/atom and Γ_{atom}^{Cr} to be 1.09×10^{-12} erg/atom. On a per atom basis, $\Gamma^* = \Gamma_{atom}^{Cr} / \Gamma_{atom}^{Ni} = 1.14$ as contrasted to

Fig. 3-3 A plot of surface tension ratio versus atomic size ratio showing that Ni (for the NiCr systems) and Fe (for the ZrFe systems) segregation is expected if solid surface tension per atom ratio is used but that Cr and Zr segregation is expected when the surface tension ratio from liquids is used. The area inside (outside) the bond breaking + non-linear elasticity envelope denotes expected solvent (solute) enrichment at surface (based upon the model in ref 36)

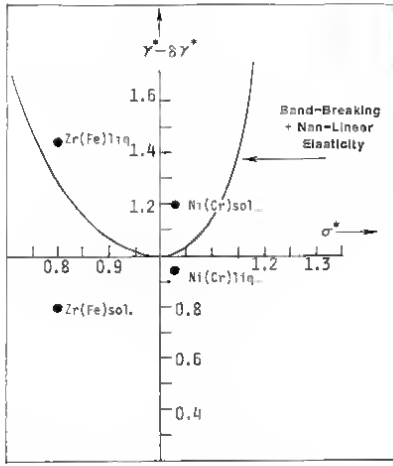
$\gamma^* - \delta\gamma^*$
1.6
1.4
1.2
Zr(Fe)liq.
Ni(Cr)sol.
Band-Breaking
+ Non-Linear
Elasticity
σ^*
0.8
0.9
1.2
1.3
Ni(Cr)liq.
Zr(Fe)sol.
0.8
0.6
0.4

$\Gamma_{area}^{Cr} / \Gamma_{area}^{Ni} = 1.07$ on a per area basis. Therefore, calculating the surface energy ratio on a per atom basis demonstrates to an even greater extent that segregation of Ni to the surface of Ni-Cr alloys is expected.

A second example, the Zr(Fe) system, can be cited to illustrate the importance of using solid surface energy per atom rather than liquid surface energy per unit area to predict the segregating species. The parameters of Zr and Fe are in Table 3-3. If the liquid surface energy per unit area is used, the theory of Abraham and Brundle can be used to predict segregation of Zr, but experimental data show that Fe is the segregating species (39,40). This system is an exception for their prediction, since the surface energy ratio of r^{Fe} / r^{Zr} is overestimated by using liquid Γ_{area}. However, the dilemma can be solved by using solid Γ_{atom}. Although solid Γ_{area}^{Zr} is smaller than solid Γ_{area}^{Fe}, the average surface atom density of Zr is much lower than that of Fe, and therefore Γ_{atom}^{Zr} is actually larger than Γ_{atom}^{Fe}. By combining the Seitz radius ratio σ^* and solid surface energy ratio, r^* (per atom), Abraham and Brundle's theory then can be used to correctly predict that Fe is the segregating species as shown in Fig 3-2.

Table 3-1. Parameters Used in Equation [3-1]

$I^0_{Cr}(38\ eV)/I^0_{Ni}(61\ eV)$	1.49
$K_{Cr}\ /\ K_{Ni}$	1
$Q_{Cr}(38\ eV)$	1.6 ML
$Q_{Ni}(61\ eV)$	1.7 ML
$\overline{\cos\theta}$	0.7

Table 3-2, Atomic Radii and Volumes Surface Energies and Energy of Mixing for the Ni-Cr System

Seitz radius ratio	$\sigma^* = r_s^{Cr} / r_s^{Ni} = 1.03$
liquid surface energy (39,41)	$\Gamma_{Cr} = 1590 \pm NA$ (erg/cm^2)
	$\Gamma_{Ni} = 1780 \pm NA$ (erg/cm^2)
	$\Gamma^* = \Gamma_{Cr}/\Gamma_{Ni} = 0.89$
solid surface energy (41)	$\Gamma_{Cr} = 2090 \pm 20$ (erg/cm^2)
	$\Gamma_{Ni} = 1940 \pm 40$ (erg/cm^2)
	$\Gamma^* = \Gamma_{Cr} / \Gamma_{Ni} = 1.08$
energy of mixing correction (37)	$\delta\Gamma^* = -0.06$
atomic volume	$V_{Cr} = 7.23$ (cm^3/mole)
	$V_{Ni} = 6.59$ (cm^3/mole)
solid surface energy ratio (per atom)	$\Gamma^* = \Gamma_{atom}^{Cr} / \Gamma_{atom}^{Ni} = 1.14$

Table 3-3. Atomic Radii and Volumes, Surface Energies and Energy of Mixing for the Fe-Zr System.

Seitz radius ratio	$\sigma^* = r_s^{Fe} / r_s^{Zr} = 0.8$
liquid surface energy (38,41)	$\Gamma_{Fe} = 1910 \pm NA$ (erg/cm^2)
	$\Gamma_{Zr} = 1480 \pm NA$ (erg/cm^2)
	$\Gamma^* = \Gamma_{Fe} / \Gamma_{Zr} = 1.27$
solid surface energy (41)	$\Gamma_{Fe} = 1910 \pm 190$ (erg/cm^2)
	$\Gamma_{Zr} = 1850 \pm NA$ (erg/cm^2)
	$\Gamma^* = \Gamma_{Fe} / \Gamma_{Zr} = 1.03$
energy of mixing correction (37)	$\delta\Gamma^* = -0.15$
atomic volume	$V_{Fe} = 7.1$ (cm^3/mole)
	$V_{Zr} = 14.1$ (cm^3/mole)
average surface atom density	$N_{Fe} = 1.93 \times 10^{15}$ (atoms/cm^2)
	$N_{Zr} = 1.22 \times 10^{15}$ (atoms/cm^2)
solid surface energy ratio (per atom)	$\Gamma^* = \Gamma_{atom}^{Fe} / \Gamma_{atom}^{Zr} = 0.5$

Compositional Changes Induced by Ion bombardment

Results

The Ni-15%Cr (110) surface was sputtered at room and elevated temperatures by Ar^+ with an energy of 2 keV and a current density of 1-2 $\mu A/cm^2$. The changes in surface composition during ion-bombardment were monitored by AES. Prior to sputtering, the sample was sputter cleaned and annealed at 650°C for 30 minutes, then slowly cooled to the desired temperature. Though the segregation of Ni is expected to be greater at lower temperature, the starting Ni compositions at temperatures between 400°C and 25°C were only slightly lower than that of 500°C because of the slow diffusion preventing achievement of equilibrium segregation. The low energy Auger Cr(38 eV)/Ni(63 eV) peak-to-peak ratio as a function of sputtering time is shown in Fig 3-4. With respect to the starting ration, the Cr/Ni ratios were increased by ion bombardment at all temperatures except at 650°C where a constant ratio was observed. The time required for Cr/Ni ratio to reach a steady state was also increased as the temperature increased. For 400°C and 500°C, the time to reach steady state was quite long and steady state conditions were not reached in some cases. For substrate temperatures over 550°C the situation was reversed and the time to reach steady state actually decreased.

Discussion

These results generally are consistent with the model of preferential sputtering proposed by Swartzfager and co-workers (42)

Fig. 3-6 The ratios of Cr(38 eV) to Ni(61 eV) Auger peak-to-peak height as function of sputtering time at room and elevated temperatures.

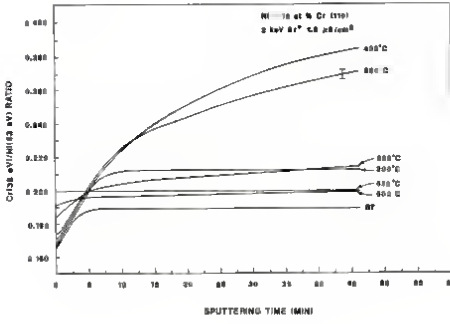
Ni 10 at % Cr (110)
2 keV Ar+ 5.0 μA/cm²
400°C
300°C
200°C
200°C
RT
Cr/Ni 461/848 eV RATIO
SPUTTERING TIME (MIN)

Swartzfager et al. proposed that sputter-enhanced diffusion and thermodynamic forces responsible for surface segregation are the major factors that control surface composition of alloys under steady state ion-bombardment conditions. For ion-bombarded specimens, diffusion in the bulk region is expected to be slow compared to the sputter removal rate. A very steep concentration gradient will result with mass transport largely confined to the ion damage region where the high defect density will lead to enhanced diffusion rates.

From the regular solution approximation for Gibbsian segregation, if there is an enthalpy change associated with the exchange of an A atom on the surface with a B atom in the bulk, the surface composition can be expressed as [43,44]

$$(C_{A(s)} / C_{B(s)}) = (C_{A(b)} / C_{B(b)}) \exp(Q/RT), \qquad [3-5]$$

where Q is the heat of segregation, $C_{i(s)}$ is surface concentration and $C_{i(b)}$ is the bulk concentration of component i.

The steady-state surface composition during sputtering can be obtained from the conservation relation

$$(C_{A(s)} / C_{B(s)}) (Y_A / Y_B) = (C_{A(b)} / C_{B(b)}), \qquad [3-6]$$

where Y_i is the sputter yield for ions impinging on the component i in the target. If there is no phase change or precipitates in the

surface region for sputtering energies significantly above threshold energies (Y_A / Y_B) is the steady state approaches unity, and thus $C_{i(s)} = C_{i(b)}$.

For Gibbsian segregation, the surface composition $C_{i(s)}$ can be related to the subsurface composition $C_{i(sub)}$ by equation [3-7]:

$$(C_{A(s)} / C_{B(s)}) = (C_{A(sub)} / C_{B(sub)}) \exp(Q/RT) \qquad [3-7]$$

Combining the equations [3-6] and [3-7], the steady-state subsurface composition can be expressed as

$$(C_{A(sub)} / C_{B(sub)}) = (C_{A(b)} / C_{B(b)}) (Y_B / Y_A) \exp(-Q/RT) \qquad [3-8]$$

Thus the subsurface layer is expected to be depleted of the component which segregates. For the case of NiCr alloy, the segregation of Ni to the surface in vacuum can lead to Cr surface enrichment after sputtering.

The thickness of altered layer δ generally is related to enhanced diffusion and the sputter removal rate. As temperature increases, the defects reduced by ion bombardment can migrate longer distances before being eliminated by recombination or by annihilation at sinks (45). Thus, segregation can occur over a significant distance at elevated temperature. If the altered layer thickness δ,

is much larger than the interplanar spacing, δ can be expressed as (42,46).

$$\delta = D / I^{+}V, \qquad [3\text{-}9]$$

where D is the diffusion rate, I^{+} is the ion dose rate and V is the sputter velocity. The $I^{+}V$ is expected not to vary much between room temperature and 650°C, but D is increased by the increase of temperature, and the thickness of the altered layer will be increased proportionately to the diffusion rate. The higher steady-state Cr/Ni ratio at higher temperatures is attributed to an increased altered-layer thickness. However, the driving force for segregation, Q/RT, is decreased at higher temperatures. As a result, the surface composition is expected to approach the bulk composition at higher temperatures, which explains the decrease of Cr/Ni ratio at temperatures higher than 400°C.

For the present case since the steady-state ratio at room temperature is lower than that of 650 °C, it appears that the room temperature sputtered surface is depleted of Cr rather than Ni. The XPS Cr/Ni ($2p_{3/2}$) peak area ratio of a poly-crystalline NiCr sample after 4 keV, 1.5 μA Ar^{+} sputtering for 30 minutes is shown in Fig. 3-5. The slight decrease of Cr/Ni ratio at 20° again suggests the depletion of Cr in the subsurface region. One reasonable explanation for the depletion of Cr is due to the low diffusion rate at room temperature, which does not allow the surface segregation lead to the

depletion of Ni. Since no impurity other than Ar was detected by AES on sputtered surface the possibility of influence by contaminants on surface composition can be excluded.

In order to quantify the AEXPS data, an iterative procedure developed by Bussing and Holloway [47] was employed to determine a least squares curve-fit of the data using summation of the Laplace transformations of step functions to yield the composition profile. As shown in Fig.3-6, the calculated composition depth profile shows depletion of Cr region below the first third monolayer if Ω_{Cr} is assumed to be 4 ML (~9 Å). In addition, the calculated compositions in the first layer is equal to the bulk composition which agrees with the result ($C_{i(s)} = C_{i(b)}$) predicted from equation [3-6].

If a collision cascade is initiated in a solid with atoms of different masses and surface binding energies, the momentum and energy will be distributed differently to each constituent resulting in different ejection probabilities for the atoms. Sigmund [49] has shown the cascade sputtering ion yield ratio of a binary alloy can be written as

$$(S_A / S_B)_{cascade} = (M_B / M_A)^{2m} \cdot (U_B / U_A)^{1-2m} \qquad [3-12]$$

where S_i is the partial sputtering yield, M_i is the atomic mass, U_i is the surface binding energy and m is the power cross section exponent. The exact value of the parameter m is uncertain since m depends upon the energy. At higher energies (> 100 keV) m = 1, while

Fig 3-5 The Cr to Ni peak area ratios of NiCr sputtered at room temperature versus take-off angle and the least squares curve-fit data, where $R(\theta) = I_{Cr}/I_{Ni}$.

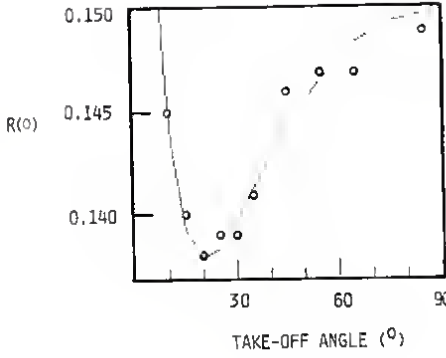
0.150
0.145
0.140
R(o)
30
60
90
TAKE-OFF ANGLE (°)

Fig. 3-6 The derived composition profile fore Fig. 3-5, where $C_{Cr} = n_{Cr}/(n_{Cr} + n_{Ni})$ and x/Ω = relative depth with respect to the escape depth of photoelectron.

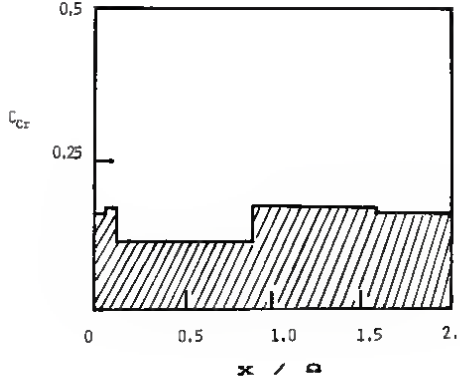
0,5
C_{cr}
0.25
0
0.5
1.0
1.5
2.0
x / a

for medium energies (10 to 100 keV) $m \approx 0.5$ and for the energies used in this study (< 10 keV) $0 \leq m \leq 0,5$ (48). At low energies, equation [3-12] shows a weak dependence on the mass ratio and a much stronger dependence on the binding energy ratio. In the case of binary alloys the surface binding energy, U_i, of a metal atom is usually taken to be equal to the sublimation energy, ΔH_i^s, of the metal (49,50).

The local temperature of a solid may be increased drametically in a very short time (~100 ps) due to elastic collisions. As a result atoms can be thermally evaporated by this sudden increase of temperature (thermal spike). The thermal sputtering ion yield ratio can be expressed as (51)

$$\left(S_A / S_B\right)_{thermal} = \left(\Gamma_A X_A / \Gamma_B X_B\right) \cdot \left(M_B / M_A\right)^{1/2} \cdot \left(\Delta H_B / \Delta H_A\right)^2 \cdot \exp\left[\left(\Delta H_B - \Delta H_A\right) / kT_{spike}\right], \qquad [3\text{-}13]$$

where Γ_i is the thermodynamic activity coefficient, ΔH_i is the heat of atomization and T_{spike} is the "thermal spike temperature".

As pointed out by Kelly (51) $\left(S_A / S_B\right)_{thermal}$ ratio can be different from unity, but the absolute values of $S_{thermal}$ are very small for alloys. The yields for cascade sputtering are expected to be much more important than thermal sputtering in alloys (51).

For those systems showing either no segregation or weak segregation, other sputtering mechanisms like cascade sputtering are the competing factors with surface segregation for preferential sputtering. The heat of segregation of Ni(Cr) and some frequently

studied systems (52) are listed in Table 3-4 in which as compared with other systems Ni is only weakly segregated to NiCr surface. This indicates that cascade sputtering cannot be totally ignored in NiCr system.

From equation [3-12] with $(U_{Cr} / U_{Ni}) = (W^{\circ}_{Cr} / W^{\circ}_{Ni}) = (95.0$ kcal/mole / 102.8 kcal/mole) = 0.92 (53), $(S_{Ni} / S_{Cr})_{cascade}$ is calculated to be 0.92 - 0.89 (for n = 0 to 0.5 respectively). The value for $(S_{Ni} / S_{Cr})_{cascade}$ is less than unity which suggests that Cr can be preferentially sputtered from NiCr alloy in agreement with experimental observation.

Table 3-4. Heats of Segregation for NiCr and Other Systems (52)

Alloy	solvent(solute)	segregating element	heat of segregation (Kcal/mole)
	Ni(Cr)	Ni	2.5
	Ni(Cu)	Cu	-5.7
	Ni(Au)	Au	-20.5
	Ni(Pd)	Pd	-10.6
	Ag(Au)	Ag	5.1
	Cu(Au)	Au	-6.1

Summary

The equilibrium surface segregation of an atomically clean binary Ni-15%Cr(110) was studied using AES. It was shown that Ni segregated preferentially to the surface in vacuum at temperatures between 500 and 650°C with a heat of segregation of 2550 cal/mole. Based on theoretical models and liquid surface energy per unit area which are commonly used to predict the segregating species, Cr rather than Ni would be expected to segregate. This system and these data demonstrate two important points: first, the surface energy of solids rather than liquids must be used to properly predict surface segregation; and second, the segregating species should be predicted based upon the surface energy per unit atom rather than on the basis of per unit area.

The compositional changes of NiCr alloys during ion-bombardment were also studied using AES and XPS. As the sputtering temperature increased, the steady-state Cr/Ni ratio increased continuously from 200°C to 400°C. Above 400°C, the steady-state Cr/Ni ratio decreased with increasing temperature. Compositional changes result from preferential sputtering of Ni caused by the surface segregation of Ni and radiation-enhanced diffusion. In contrast to elevated temperatures, the composition depth profile of room temperature sputtered NiCr alloy shows that the subsurface region is depleted of Cr instead of Ni. This can be due to low diffusion rates at room

temperature, and surface segregation cannot fully occur to deplete Ni. The cascade sputtering yield ratio of Ni to Cr is calculated to be less than unity which may explain the depletion of Cr on sputtered NiCr surface at room temperature.

CHAPTER 4
KINETICS OF OXYGEN UPTAKE

Results and Discussion

Adsorption of Oxygen

Oxygen uptakes on sputtered clean polycrystalline Ni, Cr and NiCr alloy were measured at 300 °K with XPS using the O(1s) peak area and are depicted in Fig 4-1. Three different reaction regions as previously reported (54,55,56) can be distinguished for oxygen on pure Ni: (1) a rapid increase of oxygen signal intensity over the first 5 L of exposure due to dissociative chemisorption of oxygen (2) a plateau between 10 to 20 L of oxygen exposure interpreted as saturation of the chemisorbed layer and nucleation of NiO, and (3) a relatively constant increase of oxygen up to ~100L due to growth of NiO island on the surface. The reaction of oxygen with Cr surface (57) also has been found to occur in three stages, but the initial rate of oxygen up-take and the saturated oxygen concentration are both higher than for Ni. In addition the plateau in the oxygen uptake curve of Ni does not appear in the uptake curve of Cr suggesting that the chemisorbed layer does not passivate as well and that oxide nucleates much more readily on Cr than Ni

Though the NiCr alloy contains more Ni than Cr the shape of uptake curve of NiCr alloy appears similar to pure Cr. Following a rapid increase of oxygen signal over the first ~20 L of exposure, a

Fig. 4-1 XPS O(1s) peak areas versus oxygen exposure for polycrystalline pure Ni, pure Cr and NiCr alloy at room temperature.

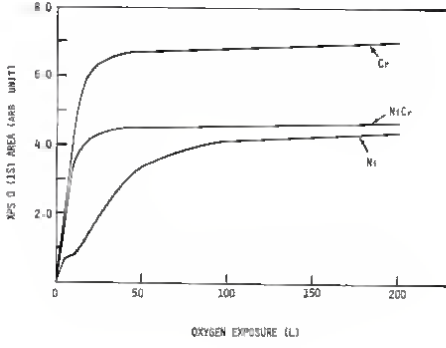
8.0
6.0
4.0
2.0
0
50
100
150
200
XPS O (1S) AREA (ARB UNIT)
OXYGEN EXPOSURE (L)
Cr
Ni+Cr
Ni

saturation value is soon reached, and no plateau in the oxygen uptake curve is observed. The saturated surface oxygen concentration on NiCr alloy, which is above that of pure Ni but below that of Cr, reflects the mixed natures of NiCr oxide. As concluded later in chapters 7 and 8, the resultant surface oxygen concentration of NiCr is due to a mixture of Ni hydroxide and Cr oxide in an outer oxide layer, and a discontinuous Cr oxide layer with some metallic Ni in the inner oxide layer.

Ni(2p) and Cr(2p) Spectra

The XPS Ni(2p) spectra of Ni and NiCr alloy as a function of oxygen exposure is shown in Fig 4-2. The spectra labelled 0 L represent the clean Ni and NiCr alloy surfaces. Notice the changes in the XPS spectra at larger oxygen exposure. For pure Ni, the chemically shifted peaks shown in Fig 4-2(a) are clearly evident at exposures of ≥ 30 L. The binding energy ($B.E.$) of metallic Ni $2p_{1/2}$ is at 852.2 eV, and the chemical shift of 1.5 eV is consistent with the formation of NiO. As compared to pure Ni, nickel in NiCr alloy exhibits a higher oxidation rate; its chemical shifted peak (binding energy is at 855.6 eV) becomes visible at oxygen exposure as low as 10 L as shown in Fig 4-2(b). The assignment of this chemically shifted Ni peak has been a subject of controversy. The detailed discussions of the assignments of O(1s) and Ni(2p) spectra will be presented in chapter 5 and 6, respectively. According to the conclusions of chapters 6, the chemically shifted Ni($2p_{1/2}$) peak on

Fig. 4-2 XPS Ni(2p) spectra as a function of oxygen exposure at room temperature for polycrystalline (a) pure Ni and (b) NiCr surface.

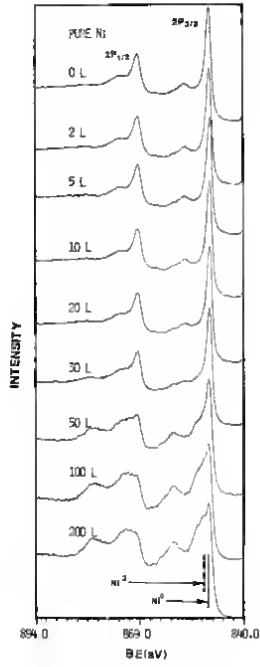

FIG.4-2(a)
(continued)

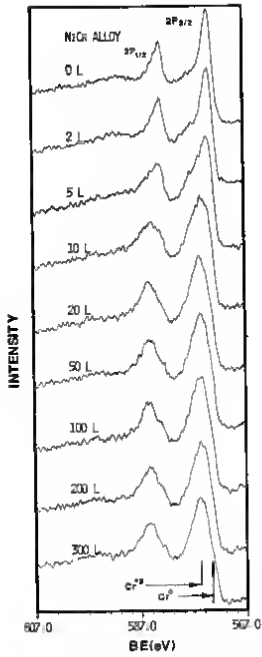
Ni3Cr ALLOY
2P3/2
2P1/2
0 L
2 L
5 L
10 L
20 L
50 L
100 L
200 L
300 L
Cr+3
Cr0
INTENSITY
607.0
597.0
587.0
BE(eV)

FIG.4-2(b)

NiCr alloy does not correspond to the formation of NiO or Ni_2O_3 but to Ni hydroxide.

The XPS Cr(2p) spectra of pure Cr and NiCr alloy are shown in Fig. 4-3. Chromium in the NiCr alloy is oxidized more rapidly than pure Cr. Chemically shifted Cr 2p peaks become detectable at 5 L as compared to ≥ 10 L for pure Cr. Unlike the oxidation of Ni, no controversy about the assignment of the room temperature oxidation product for Cr has been reported. Though the published results show considerable variability owing to the cleanliness of the samples, pure Cr always oxidizes to Cr_2O_3. The $Cr(2p_{1/2})$ spectra of NiCr alloy had a chemical shift of .2.3 eV which is also consistent with the formation of Cr_2O_3 (57,58,59). The metallic Cr spectra from the substrate is attenuated by formation of the oxide layer. The metallic Cr peak is hardly detectable in the spectrum of the NiCr alloy after 300 L of oxygen exposure, but the pure Cr spectrum exhibits a large metallic Cr peak. The larger attenuation of Cr metallic peak on NiCr than on pure Cr suggests that Cr atoms probably segregate from deeper substrate layer to surface region to react with oxygen to form Cr_2O_3 (see chapter 8). The small metallic Cr(2p) spectrum observed on oxidized NiCr alloy results from the depletion of Cr in the metallic substrate layer next to oxide.

Both Ni and Cr in NiCr alloy are oxidized more rapidly than pure metals, which demonstrates the effects of alloying of Cr to Ni. As found in Fig. 4-2(b) and 4-3(b), Cr is oxidized preferentially in the first 10 L on the NiCr alloy surface, so it is not surprising to find

Fig. 4-3 XPS Cr(2p) spectra as a function of oxygen exposure at room temperature for polycrystalline (a) pure Cr and (b) NiCr surface.

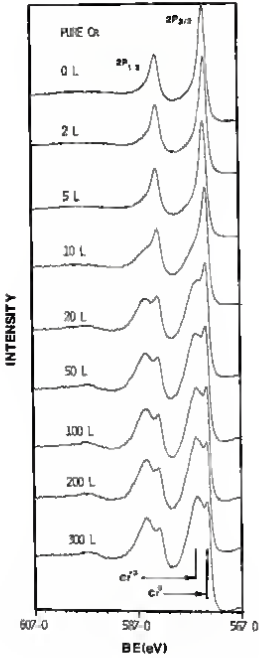

FIG. 4-3(a)

(continued)

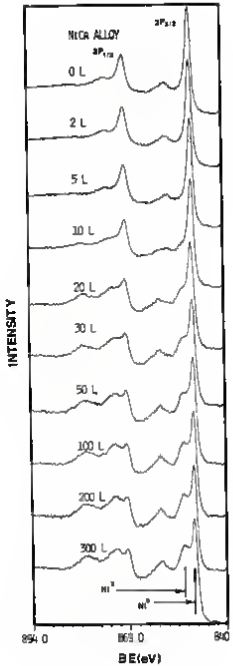
NiCr ALLOY
$2P_{3/2}$
$2P_{1/2}$
0 L
2 L
5 L
10 L
20 L
30 L
50 L
100 L
200 L
300 L
Ni^{2+}
Ni^{0}
INTENSITY
894.0
869.0
840.0
BE(eV)

FIG.4-3(b)

that the oxygen uptake curve of NiCr is very similar to that of pure Cr, rather than pure Ni in this range of oxygen exposure. Moreover, in the beginning of oxygen exposure (.5 L) the slope of oxygen uptake curves of NiCr is very close to that of pure Cr suggesting that the dissociation and chemisorption of oxygen on Cr sites probably dominate the oxidation reaction on alloy surface. The above results and observations perhaps can be qualitatively understood by the larger chemisorption energy and oxide formation energy of Cr-O system than Ni-O system [60] as shown in Table 4-1

Summary

In summary, both Ni and Cr in NiCr alloy are oxidized more rapidly than pure metals and the oxygen uptake behavior of NiCr alloy is dominated by the oxidation of Cr in the first 10 L of oxygen exposure. Both pure Cr and Cr in NiCr alloy have the same oxidation product (Cr_2O_3). In contrast to the formation of NiO on pure Ni, Ni hydroxide is found on the oxidized NiCr surface.

Table 4-1 Heats of Oxygen Adsorption and Formation of Oxide for Ni and Cr at 300°K. (from 60)

element	initial heat of adsorption (kJ/mole)	heat of formation of oxide (kJ/mole)
Cr	731	756
Ni	449	487

CHAPTER 5
ASSIGNMENTS OF XPS O(1s) SPECTRA

Introduction

As already pointed out by many authors [61,62,63,64] the assignment of various core level shifts, namely XPS O(1s) and Ni(2p) spectra, in the oxygen-nickel system is a controversial subject. This is particularly true for O(1s) emission. In contrast to the Ni-O system it has been found that only one oxidation product Cr_2O_3 formed on the room temperature oxidized pure Cr surface in UHV chamber [65,66,67].

Results

A sequence of O(1s) spectra as obtained from a Ni(110) surface after different oxygen exposures at room temperature is shown in Fig 5-1. All the O(1s) spectra, even at exposure ≤ 3 L, have a major feature at 529.0 ± 0.4 eV and a less intense feature at 530.6 ± 0.4 eV. The binding energies of the two O(1s) peaks reported here are slightly lower than previously reported binding energies which are at 529.4 ± 0.4 eV and 531.0 ± 0.4 eV respectively [68,69,70]. The discrepancy (.0.6 eV) was believed to result from the calibration of the analyzer.

Fig. 5-1 XPS O(1s) spectra of Ni(110) surface as a function of oxygen exposure at room temperature

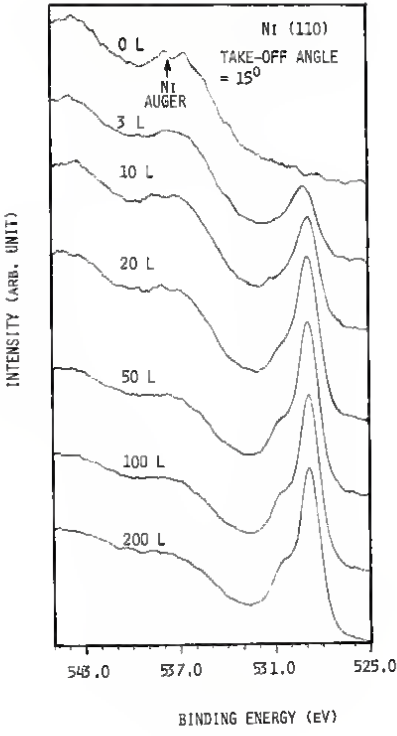
Ni (110)
TAKE-OFF ANGLE
= 15°
0 L
Ni
AUGER
3 L
10 L
20 L
50 L
100 L
200 L
INTENSITY (ARB. UNIT)
545.0
537.0
531.0
525.0
BINDING ENERGY (eV)

Discussion

The O(1s) peak at 529.0 eV has been generally reported to result from stoichiometric NiO at oxide covered Ni surfaces (68,69,70,71,72), and the high B.E. O(1s) peak has been assigned to a variety of different species such as Ni_2O_3 (68), chemisorbed oxygen (73), CO_3 (74) or hydroxyl species (75). While at low coverages (chemisorption stage) the O(1s) peaks at 529.0 eV and 530.6 eV have been assigned respectively, to (a) C(2x2) and P(2x2) (70); (b) O^{2-} and atomic O (76) (c) O^{2-} and $OH_{(ads)}$ (75) and (d) O^{2-} and CO_3 (74). One of the reasons for the inconsistent assignments is the insufficiently controlled experimental parameters, especially the composition of residual gas and perfection of surface. Another more fundamental reason, as pointed out by Wandelt (62), perhaps is that the electronic structure of chemisorbed oxygen, in particular its degree of ionicity, is still not understood.

Assignments of High Binding Energy O(1s) Peak

Many authors (68,69,70,72) have attributed the high B.E. O(1s) peak at oxide covered surface to "Ni_2O_3" but this interpretation is not correct at low oxygen coverage. The high B.E. O(1s) peak may be a result of reactions of residual gases like hydrogen and water. The influences of residual gases on the oxidation products of Ni are often ignored. For instance, Kim and Winograd (KW) (69) reported that

evaporated Ni films exposed to 100 Torr oxygen for 2 hours at room temperature had two O(1s) peaks of about equal size at 529.9 eV and 531.7 eV. The O(1s) peak at higher B.E. was attributed to defective Ni_2O_3, because KW were able to populate this high B.E. peak by bombarding a Ni surface with 400 eV O_2^+ ions. These data are not conclusive because of the poor oxygen purity. The base pressure of their vacuum system (typically at 2×10^{-8} Torr) was not in the UHV range and "water is the major contaminant with O_2" (69). Actually, the existence of (OH) species in KW's work is suggested because the XPS O(1s) and Ni(2p) line shapes of "Ni_2O_3" are similar to those of $Ni(OH)_2$ as shown in Fig. 5-2.

Factors other than impurities and bombardment were reported to have effects on the appearance of high B.E. O(1s) peak. Norton at al. (68) found that the XPS high B.E. O(1s) peak can be enhanced by heating a room temperature oxidized Ni surface to 485°K for 10 - 15 minutes or carrying out the oxidation at 485°K. Kim and Winograd (69) also reported an increase in the high B.E. O(1s) peak along with a shift of the Ni L_3VV transition when the oxidation experiment was performed at a slightly elevated temperature (between 150°C and 250°C).

Norton et al. (68) interpreted the increase of high B.E. O(1s) peak at moderate temperature to be due to the formation of Ni^{3+} or more specifically Ni_2O_3. According to the results of Norton et al., the UPS spectra of 'Ni_2O_3" formed at moderate temperature are different from Ni surface oxidized in moist O_2, so that the changes

Fig 5-2 Compilation of O(1s) and Ni($2p_{3/2}$) XPS spectra for Ni(100), various Ni oxides and Ni(100) after various oxygen exposures. For the Ni(100) + O_2 spectra the intensity scales are as marked. For the oxides the scales are arbitrary. (from ref #2, reprinted with permission

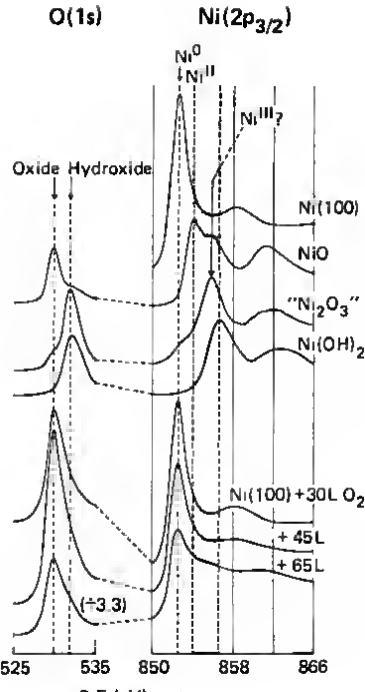
O(1s)
Ni(2p3/2)
Ni0
NiII
NiIII?
Oxide
Hydroxide
Ni(100)
NiO
"Ni2O3"
Ni(OH)2
Ni(100)+30L O2
+ 45L
+ 65L
(÷3.3)
525
535
850
858
866
δ E (eV)⟶

of Ni d-band UPS spectra due to the formation of $Ni(OH)_2$ appear to be quite unlikely. Particularly, $Ni(OH)_2$ is relatively unstable at elevated temperatures. The possibility due to Ni_2O_3 is also ruled out, since the formation of Ni_2O_3 (Ni : O = 1 : 1.5) requires diffusion of nickel atoms out of the NiO oxide layer (Ni : O = 1 : 1) or production of excess oxygen in the oxide layer; both are contrary to the result of annealing experiments, which shows heating the oxidized Ni can cause the dissolution of oxygen into bulk and reduction of NiO (77). It seems that a species other than NiO, $Ni(OH)_2$ or Ni_2O_3 is responsible for the increase of high B.E. O(1s) peak on the annealed oxidized Ni surface, but the origin of this temperature related binding energy shift phenomena still needs further study.

Identification of O(1s) Spectra by Multi-techniques Analysis

It is of interest to find just by summarizing the results from the two papers mentioned above (68,69), that high B.E. O(1s) peak can be produced by bombarding Ni with O^{2-} ion, oxidizing Ni at moderate temperatures, exposing Ni to moist O_2, exposing Ni to air, annealing the room temperature oxidized Ni, or simply oxidizing Ni at room temperature. Apart from these means, it was reported that high B.E. O(1s) can also be produced by reaction of Ni with CO_2 or H_2O (74,75) and by sputtering cleaved NiO with Ar^+ (78). It is noted that all the high B.E. O(1s) peaks mentioned have similar binding energies (531 ± 0.5 eV), even though they can be quite different species.

These results not only reveal the complexity of the assignment

of O(1s) but also demonstrate the incapabilities of XPS O(1s) data alone to resolve different O-containing species. Therefore two points are apparent: first, even though the binding energies of O(1s) may be the same, it is inappropriate to assign the O(1s) spectra by directly using the assignments obtained under different experimental conditions. Second, in order to unambiguously identify the various reaction products of Ni in Ni-O system, multi-technique analysis is needed.

Specifically for the room temperature oxidation of Ni, Hopster and Brundle (75) used SIMS and XPS to study the origins of high B.E. O(1s) peak. By correlating the high B.E. O(1s) peak with the appearance of the (OM) containing ion clusters, like OH^+ and $NiOH^+$ ions, obtained from SIMS, they concluded that the high B.E. O(1s) peak is not representative of P(2x2) Ni_2O_3 or molecular oxygen, but represents an OH species formed by reaction of oxygen with contaminated background water in UHV chamber. In addition, they also concluded that chemisorbed O, of either C(2x2), P(2x2) or other chemisorbed structures, have the same B.E. (within ±0.3 eV) as NiO.

Because of the sensitivity of electron stimulated ion desorption (ESID) technique to hydrogen (78-81), the formation of hydroxyl species during oxygen exposure was also studied by ESID in this work. The ESID results (see chapter 8) support the existence of hydroxyl groups on oxidized Ni surface.

Thermodynamic Basis for the Assignment of O(1s) Spectra

In order to understand why high B.E. O(1s) peak formed on room temperature oxidized Ni surface, it is instructive to examine the O(1s) spectra of other oxidized transition metals like chromium and iron. Chromium has two states, +3 and +6, and Fe has +8/3 and +3 states besides the lowest +2 state. If the high B.E. O(1s) shoulder on oxidized Ni is really due to the presence of oxide of higher state, Ni_2O_3, it is reasonable to expect that the high B.E. peak should also appear in the O(1s) spectra of oxidized Cr and Fe. However, as shown in the Fig. 10-5 no high B.E. O(1s) peak is observed on oxidized Cr surface. Moreover, the O(1s) spectra of oxidized Fe published by Grundle et al. (62) also do not exhibit any high B.E. shoulder peak. These experimental observations clearly indicate that the high B.E. O(1s) shoulder cannot be due to the formation of oxide of higher state.

The bonding energies of OH-metals and O-metals for Ni, Cr and Fe are listed in Table 10-1. As compared to oxygen, (OH) is not favored to bond to either Cr or Fe (for example, the bonding energies for Cr-O is -383 kJ/mole and Cr-OH is -356 kJ/mole). Even in the presence of hydrogen and water with oxygen, both Cr oxide and Fe oxide are thermodynamically more favored to form than hydroxides at room temperature. On the contrary, Ni has similar affinities to both (OH) and O, and the reaction product whether it is hydroxide, adsorbed (OH), oxyhydroxide, or oxide mainly depends upon the contents of water or hydrogen in the oxidizing environment. Under the present

oxygen exposure conditions, since hydrogen content is high (59% of the partial pressure of oxygen, see chapter 2), both hydroxyl and oxide species are expect to co-exist on Ni surface.

Summary

Two XPS O(1s) peaks (binding energies at 529.0 ± 0.4 eV and 530.6 ± 0.4 eV) were found on oxidized Ni surface. The existence of Ni^{3+} (or "Ni_2O_3") has been proposed to account for the presence of high B.E. O(1s) peak on room temperature oxidized Ni surface. However Ni^{2+} is generally considered as the only stable oxidation state in equilibrium conditions and Ni_2O_3 as a product of oxidation of Ni at room temperature is not supported by any convincing experimental results. It has been shown that the high B.E. O(1s) peak at room temperature oxidized Ni surface is due to (OH) species, and the low B.E. O(1s) peak is either due to adsorbed oxygen or NiO

CHAPTER 6
IDENTIFICATION OF THE REACTION PRODUCTS OF Ni

Introduction

In the presence of H_2O and N_2, the oxidation reaction on Ni surface can be quite complicated. Besides NiO, complicated products, such as NiO(OH), $Ni(OH)_2$ and $(OH)_{ads}$ may also be formed at surface.

Though XPS O(1s) spectra have standard Gaussian peak shapes the O(1s) spectra of many different chemical species have the same binding energy as discussed in the chapter 5. It is therefore difficult to use O(1s) spectra alone to identify the various possible oxidation reaction products, such as, $(OH)_{ads}$, $Ni(OH)_2$, NiOOH and O_{ads} or OH for the present case.

Spectra from Ni(2p) have more complicated line shapes than O(1s) spectra. If more than one reaction product exists it is apparently not a trivial work to accurately estimate the composition of different mixed reaction products of Ni formed on the oxidized Ni or NiCr surfaces. Successful curve fitting analysis of Ni(2p) spectra of a selected mixed Ni/Al_2O_3 system has been demonstrated (83). However the curve fitting analysis is considerably more difficult for the present case, simply because more chemical species are present on Ni and NiCr surfaces oxidized at room temperature.

Spectra from XPS of metallic Ni(2p) and its oxide compounds

generally exhibit a main peak and some satellite fine structures as illustrated in Fig.5-2. The satellites occur either from extrinsic energy-loss processes as the primary electrons pass through the sample or from intrinsic energy-loss processes during photoemission events (84). For a simple mixed oxidation product system like NiO and $Ni(OH)_2$, the overlaps of satellites with major peaks cause difficulties in deconvolution. With respect to the B.E. of metallic Ni at 852.2 eV, the major peak of $Ni(OH)_2$ is at ~855.6 eV, while that of NiO is at ~853.8 eV and does not overlap with the major peak of $Ni(OH)_2$. But NiO has a large multiplet splitting satellite peak beside the major peak at ~855.2 eV (85), which does overlap with the major peak of $Ni(OH)_2$. In addition, the shake-up satellite of NiO (88) at ~880.8 eV also overlaps with the shake-up satellite of $Ni(OH)_2$ at ~861.2 eV.

Because of the large FWHM (~2.5 to 5 eV) and the Doniach-Sunjic line shapes (which result from electron-hole interaction (87,88)) accurate quantification analysis of this two component mixed system is rather difficult. Moreover, the overlaps also make the identification of small amount of NiO in the presence of large amount of $Ni(OH)_2$, or vice versa, more difficult. On an oxidized Ni surface the difficulties of quantification are further enhanced by the presence of metallic Ni spectra and the complicated inelastic backgrounds, which act as possible extra sources of asymmetry for these peaks. Therefore, no attempts were made to quantify the peak areas and amounts of NiO and Ni hydroxide on oxidized Ni or Ni

surfeces.

Deepite of the difficultiee in quentitetive anelysis useful quelitetive information cen be obtained from the Ni(2p) epectre; particularly for differentieting variaus products like Ni hydroxide eed eisorbed (OH) on NiCr eed Ni surfaces, since the cheegee of Ni(2p) spectra line shapee ere more eensitive to these chemieel speciee than O(1e) epectre.

Results

The XPS Ni(2p) epectre of oxidized Ni(110) aed NiCr alloy surfecee efter 300 L ef oxygen exposure ee well ee 300 L of oxygee exposure plus air exposure are ehowe in Fig.6-1. After 300 L of oxygen exposure in UHV, the mejor oxidetion product of Ni in NiCr alloy is Ni hydroxide (the B.E. of the major peek ie et 855.6 eV) which is eppreeiely different from NiO (the B.E. of the major peek ie et 853.8 eV) formed on pure Ni. After eir exposure, ee edditioeel feature et 855.6 eV eppeers in the Ni(2p) spectre of pure Ni indicetieg the formetion of Ni hydroxide. The identificetion of Ni hydroxide of large emount in the spectra like the ehove case is eesy However the existence of other reaction products of emeller emount is not obvious due to the overlepe of peaks.

At higher teke-off engles, the intensities of the products et the outer etomic layers reletive to the products in the inner layer will be decreesed. ee engle-resolved XPS enelysee were performed to

Fig. 6-1 Ni(2p) XPS spectra at $\theta = 45°$ for (a) Ni(110) exposed to 300 L at $P_{O2} = 5 \times 10^{-8}$ Torr, (b) Ni(110) exposed to air for 5 minutes subsequent to (a), (c) polycrystalline NiCr alloy exposed to 300 L at $P_{O2} = 5 \times 10^{-8}$ Torr, (d) polycrystalline NiCr alloy exposed to air for 5 minutes subsequent to (c).

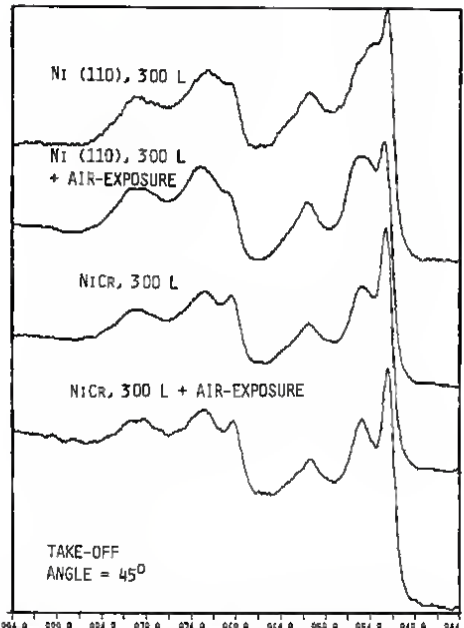
Ni (110), 300 L
Ni (110), 300 L
+ AIR-EXPOSURE
NiCr, 300 L
NiCr, 300 L + AIR-EXPOSURE
TAKE-OFF
ANGLE = 45°
894.0 889.0 884.0 879.0 874.0 869.0 864.0 859.0 854.0 849.0 844.0
BINDING ENERGY (eV)

measure the inhomogeneities of reaction products as a function of depth. The identification of reaction products of Ni is interfered by the metallic Ni spectra, particularly at high take-off angles where the intensities of metallic Ni peaks are so large and other peaks are smeared (for example, see Fig. 6-1). In order to more effectively compare the spectra taken at different take-off angles, the metallic Ni peaks are subtracted from raw spectra by the normalized metallic Ni spectra obtained from a clean Ni surface. The backgrounds of the raw spectra are also subtracted using a modified Shirley method provided by Perkin-Elmer Co. Thus, the difference Ni(2p) spectra should be only consisted of reaction products, either NiO or Ni hydroxide or a mixture of the two. This procedure allows one to amplify the spectra of reaction products at high take-off angles. The difference Ni(2p) spectra of oxidized Ni and NiCr alloy surfaces as a function of take-off angle are compared in Fig. 6-2.

Discussion

Reaction Products on Pure Ni

A. 300L + air-exposure

As shown in Fig. 6-2(a), the difference Ni(2p) spectra for 300 L plus air-exposed Ni(110) has a dominant feature due to Ni hydroxide (whose binding energy is 855.6 eV) at 15° take-off angle. As the take-off angle increases, the intensity of the NiO peak at 853.8 eV increases suggesting the existence of NiO at inner oxide layer. The enhancement of Ni hydroxide features at lower take-off angles

Fig 6-2 The difference Ni(2p) XPS spectraafter substraction of background and metallic Ni xpectra (a) Ni(110) exposed to 300 L O_2 + air (b) Ni(110) exposed to 300 L O_2; (c) NiCr alloy exposed to 300 L O_2 + air (d) NiCr alloy exposed to 300 L O_2.

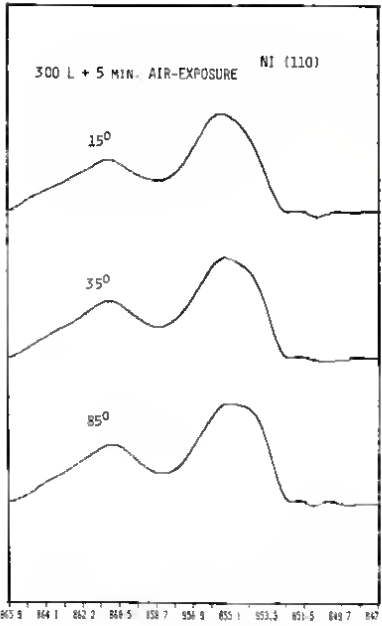

FIG.6-2 (a)

(continued)

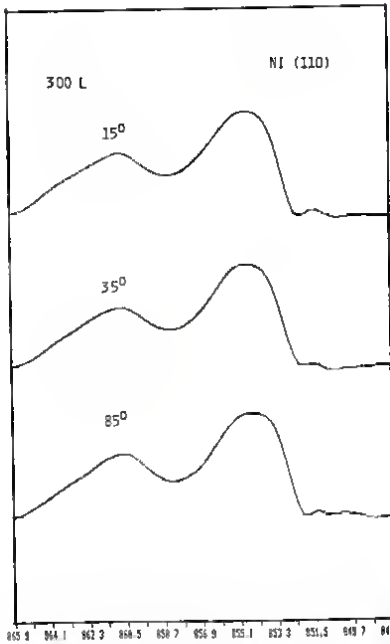

FIG 6-2 (b)

(continued)

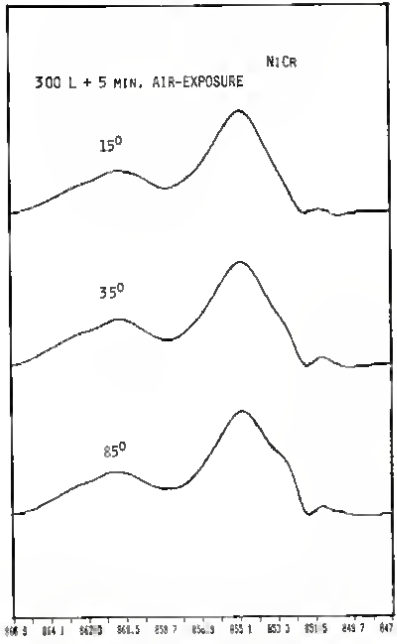

FIG 6-2 (c)
(continued)

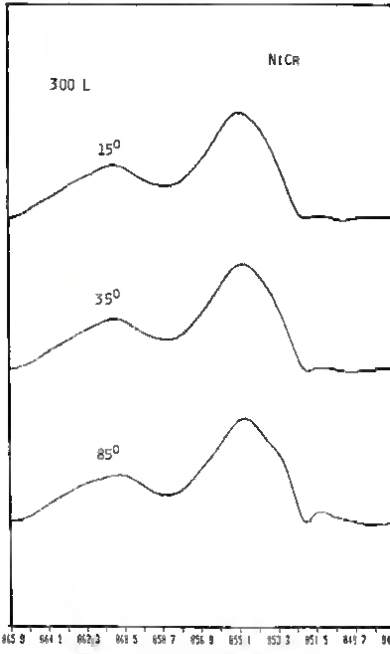
NiCr
300 L
15°
35°
85°
865.9
864.1
862.3
860.5
858.7
856.9
855.1
853.3
851.5
849.7
847.9
BINDING ENERGY (eV)

FIG 6-2 (d)

Fig 6-3 O(1s) XPS spectra versus take-off angle for Ni(110) exposed to 300 L at 5 x 10^{-8} Torr.

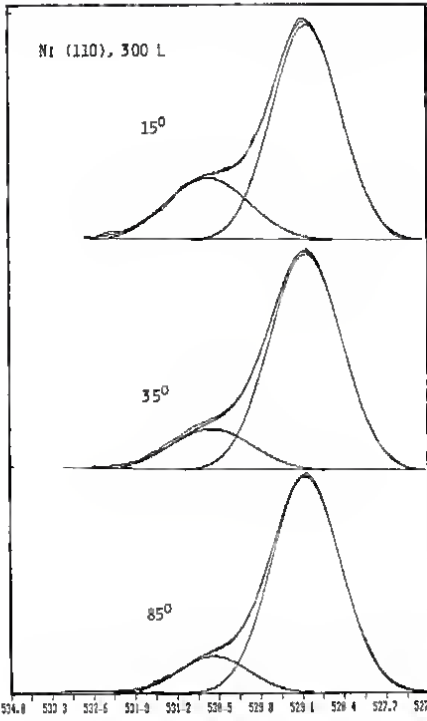
Ni (110), 300 L
15°
35°
85°
534.8 533.3 532.5 531.9 531.2 530.5 529.8 529.1 528.4 527.7 527.0
BINDING ENERGY (eV)

suggests that Ni hydroxide is concentrated at outer oxide layer. The difference spectra as a function of take-off angle in Fig 6-2(a) clearly demonstrate the existence of both NiO and Ni hydroxide on the air-exposed Ni surface.

B. 300L

The difference Ni(2p) spectra of 300 L oxidized Ni(110) surface are shown in Fig 6-2(b). In contrast to the air-exposed Ni surface, the difference spectra are unchanged as take-off angle varies. This indicates that the reaction products of Ni on the UHV oxidized Ni(110) surface is homogeneous as a function of depth. But as shown in Fig 6-3 the O(1s) spectra of 300 L oxidized Ni show substantial increases of high B.E. O(1s) peaks as take-off angles increase, indicating that the (OH) groups exist at the outer surface with respect to oxide layer. If the (OH) signals are due to the presence of Ni hydroxide, based upon the O(1s) spectra it is reasonable to expect that Ni hydroxide should exist at outer surface, and part of the difference spectra should be attributed to Ni hydroxide. The peak area of hydroxyl O(1s) is about 44% of the oxide O(1s) peak area (or 31% of the total O(1s) peak area) at 15° take-off angle. If Ni hydroxide has the chemical formula $Ni(OH)_2$, the Ni difference spectrum at 15° take-off angle would be composed of 18% of $Ni(OH)_2$ and 82% of NiO. As take-off angle increases to 85°, the relative percentage of NiO should be increased, and the Ni difference spectrum would be composed of 7% $Ni(OH)_2$ and 93% of NiO (the peak area of hydroxyl O(1s) is about 16% of the oxide O(1s) peak area). As

compared with synthetical spectra obtained by mixing the standard NiO and $Ni(OH)_2$ spectra with the same ratios, if Ni hydroxide exists at outer oxide layer the Ni difference spectra in Fig 6-2(b) should be angle-dependent This is contrary to the angle-independent Ni(2p) difference spectra in Fig. 6-2(b), indicating that Ni hydroxide is not formed on Ni surface, and the (OH) is only an adsorbed species on the Ni oxide surface. Because the dominant feature of difference spectra resides at 853.3 eV, the major oxidation product in believed to be NiO.

Reaction Products on NiCr Alloy

As shown in Fig 6-2(c) and (d), the difference spectra of both 300 L and 300 L plus air-exposed NiCr surfaces are quite similar and both spectra have a dominant feature at 855.6 eV which indicates the existence of Ni hydroxide. As take-off angle increases, a peak at 853.3 eV which is almost totally unseen at 15° take-off angle slightly increases its intensity suggesting the existence of NiO in the inner oxide layer As judged by the area of the NiO feature the amounts of NiO formed on the both 300 L and air-exposed oxidized NiCr surfaces were quite small. In addition the intensity of NiO feature on the air-exposed surface is slightly smaller than the 300 L UHV oxidized surface, which suggests that the NiO formed in UHV on NiCr surface was partially hydroxylated by moist air similar to that on pure Ni

Summary

In summary, because of the complexities of O(1s) spectra, the oxidation products of Ni on Ni and NiCr surfaces are identified by using XPS Ni(2p) spectra. After 300 L of oxygen exposure, NiO is formed on pure Ni surface, and the high B.E. O(1s) peak is due to the presence of adsorbed hydroxyl in the outer oxide layer. After exposing the 300 L oxidized Ni to air for 5 minutes, NiO is partially hydroxylated and Ni hydroxide is formed in the outer layer. Ni hydroxide and small amount of NiO in the inner oxide layer are found on both 300 L oxidized and air-exposed NiCr alloys.

CHAPTER 7
ION SCATTERING SPECTROSCOPY OF NiCr ALLOY

Results and Discussion

Components on the NiCr Surface

The ISS spectra of NiCr surface before and after room temperature oxidation are shown in Fig.7-1. Compared to the spectra of clean pure Ni and Cr, both Ni and Cr are apparently present in the top layer of clean and oxidized surfaces. An increased background or tail intensity in the lower kinetic energy region is observed in the oxidized NiCr ISS spectrum.

Only O, Ni and Cr were detected by AES on the UHV oxidized NiCr surface. Thus the broad high intensity ISS background can not be attributed to elastic scattering peaks from the elements on the surface. The possibility of high background due to the presence of surface hydrogen is also excluded because surface hydrogen only causes a reduced scattered ion yield from the substrate [89,90].

Since the high intensity tail was not seen for clean NiCr surface, this background must be associated with oxygen on the surface. The backgrounds in ISS spectra generally are due to ions which penetrate and lose energy on their inward and outward paths in additions to the energy lost in the backscattering collision. The intensity of the background is directly affected by the efficiency of

Fig. 7-1 1 keV Ne^+ ISS spectra taken from pure Ni, pure Cr clean NiCr alloy and oxidized NiCr alloy (100 L O_2 at room temperature).

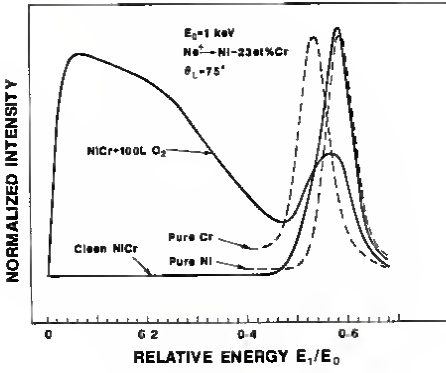
E0=1 keV
Ne+→Ni-23at%Cr
θL=75°
NiCr+100L O2
Clean NiCr
Pure Cr
Pure Ni
NORMALIZED INTENSITY
0
0.2
0.4
0.6
RELATIVE ENERGY E1/E0

ion neutralization at surface (91). As the ion neutralization efficiency decreases, the intensity of the background is expected to increase. In the presence of surface oxygen, the positive ion yields increases because less tunneling occurs to neutralize the positive ions. Therefore, it is reasonable to expect that surface oxygen may cause increased backgrounds in ISS spectra. Furthermore, even though no elastic peak from oxygen is observed, the background can be regarded as an indication of the presence of surface oxygen.

Annealing Experiment

The thermal stability of oxide of NiCr was studied by heating the sample to 500°C. When the oxidized surface was heated, AES data (see Fig 7-2) showed a continuous decrease of O(KLL) intensity accompanied by decreased background intensities in the ISS spectra as shown in Fig 7-3. It is believed that the decreased oxygen signal during heating is a result of the dissolution of surface oxygen into subsurface region (92). The correlation between AES O(KLL) signal and ISS background intensity further supports the explanation of the background as being due to surface oxygen.

Apart from decreased background during heating, ISS spectra also provide information about the changes of the surface compositions of Ni and Cr. As shown in Fig 7-3, initially the Cr signal increases and Ni signal decreases, which indicates Cr segregates to the surface. Prolonged heating at 500 °C caused a decreased Cr signal and an increased Ni signal, showing reversal of the Cr and Ni compositions

Fig 7-2 1 keV ISS spectra as a function of heating time at 500°C for NiCr alloy exposed to 100 L O_2 and 1 keV ISS spectrum of clean NiCr alloy.

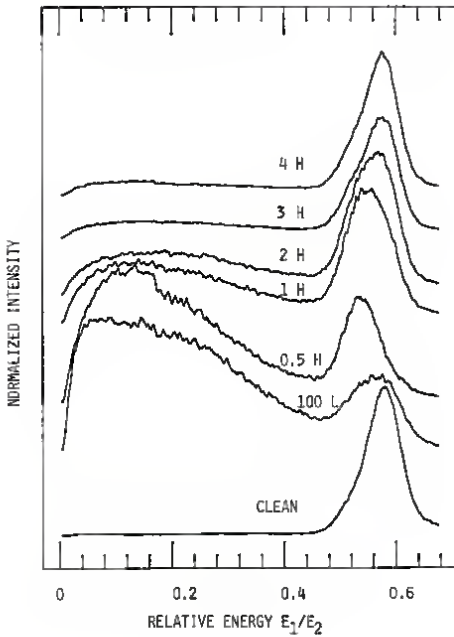
4 H
3 H
2 H
1 H
0.5 H
100 L
CLEAN
NORMALIZED INTENSITY
0
0.2
0.4
0.6
RELATIVE ENERGY E_1/E_2

Fig. 7-3 Auger peak to peak or peak to background intensities versus heating time at 500°C in vacuum.

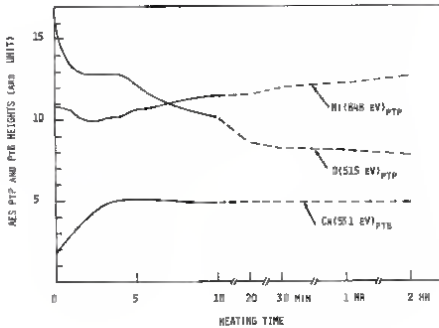
AES PTP AND PTB HEIGHTS (ARB UNITS)
15
10
5
0
5
1M
20
30 MIN
1 HR
2 HR
HEATING TIME
Ni(848 EV)PTP
P(515 EV)PTP
Ca(551 EV)PTB

in the top layer. After four hours of heating at 500 °C, ISS spectrum showed that the top layer of the oxidized NiCr alloy was almost restored back to that of the clean surface by heating, and a negligible background suggests that only a very small amount of oxygen is present in the top monolayer. But AES still detects a substantial amount of oxygen (the O KLL intensity is > 50% of the initial oxygen signal). Because of the relative long escape depth for O(KLL) Auger electron (about 8 ~ 9 ML in the oxide [92]), the discrepancy between AES and ISS results indicates some oxygen is dissolved into the subsurface region. This subsurface oxygen can be detected by AES but not by ISS.

While ISS shows the top layer surface composition is close to the clean surface, both Auger low energy and XPS 2p spectra showed that only Ni hydroxide was reduced to metallic Ni with Cr oxide being only partially reduced even after prolonged heating at 500°C for 4 hours. These results indicate that Cr oxide has better thermal stability than Ni hydroxide, and most of the dissolved subsurface oxygen is probably associated with Cr oxide not Ni; it is evident that the alloying of Cr changes the distribution of oxygen at annealed oxidized surface.

Summary

In summary, the results of ISS experiments indicate both Ni and Cr are present at oxidized NiCr surface. Though no elastic scattering

peak from oxygen atom can be detected under the present experimental conditions, the high backgrounds can serve as an indication of the presence of surface oxygen. The thermal stability of the oxides on NiCr alloy has been studied It is found that Cr oxide has better stability than Ni hydroxide at 500 °C. In addition the distribution of oxygen at annealed oxidized Ni surface is modified by the addition of Cr

CHAPTER 8
STRUCTURE OF OXIDE LAYER

In order to learn more about the structure of oxide formed on NiCr surface after 300 L of oxygen exposure, angle-resolved XPS experiments were performed.

Results

The XPS spectra of Ni(2p), Cr(2p) and O(1s) taken at different take-off angles are shown in Fig 8-1. Notice that the Ni hydroxide feature at 855.6 eV is the dominant feature at 15° take-off angle while the intensity of the Ni hydroxide decreases and metallic Ni peak becomes the major feature as the take-off angle increases to 85° (near normal from the surface). In contrast to Ni(2p) spectra Cr(2p) spectra do not change significantly as take-off angles vary. Cr oxide always is the major feature in Cr(2p) spectra even at 85° take-off angle.

A method was used which was similar to the method employed in chapter 6, and consisted of subtraction of the spectra of metallic Ni or Cr oxide from the corresponding raw spectra. The ratios of the peak areas of Cr oxide to Ni hydroxide and Cr metal to Ni metal as a function of take-off angle are plotted in Fig.8-2 with increased take-off angle, the ratios of Cr oxide to Ni hydroxide increased

Fig. 5.1 Ni(2p), Cr(2p) and O(1s) XPS spectra versus take-off angle for NiCr alloy exposed to 300 L O_2.

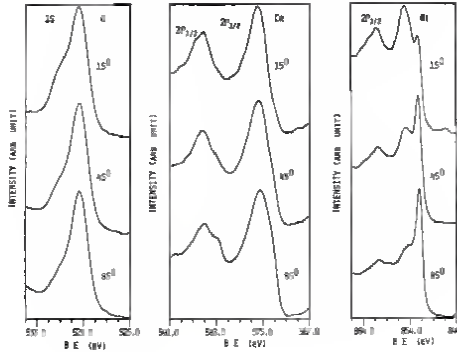
O1s
15°
45°
85°
INTENSITY (Arb. Unit)
B.E. (eV)
Cr2p3/2
Cr2p1/2
Cr
O1s

Fig 8-2 The peak area ratios of Cr oxide to Ni hydroxide and Cr metal to Ni metal versus take-off angle for NiCr alloy exposed to 300 L O_2

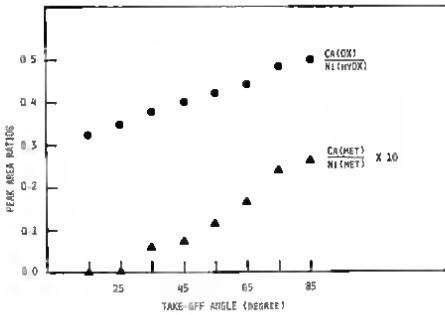
0.5
0.4
0.3
0.2
0.1
0.0
PEAK AREA RATIOS
25
45
65
85
TAKE-OFF ANGLE (DEGREE)
Ca(OX) / Ni(HYDX)
Ca(MET) / Ni(MET) X 10

suggesting that Ni hydroxide is present at the outer surface of NiCr oxide. The decreased contribution of the high B.E. O(1s) peaks to the overall O(1s) spectra as take-off angle increased in Fig 8-1 also suggest the existence of hydroxide at outer oxide layer.

The spectra of Ni(2p) and Cr(2p) of oxidized NiCr surface after sputtered by 4 keV Ar^+ for 1 minutes are shown in Fig 8-3. It can be seen that Ni hydroxide is almost completely removed, but most of Cr oxide seems to remain "intact" after sputtering. The sputtering results tend to agree with the non-destructive ARXPS results above suggesting Ni hydroxide was indeed in the outer oxide layer.

Two Layer Model

The heterogeneous oxide structure formed on NiCr surface can be quite complicated. Combined all the information obtained by ISS (chapter 7) and ARXPS, it can be concluded here that Ni hydroxide and Cr oxide are in the outer oxide layer while Cr oxide and small amount of Ni oxide are in the inner oxide layer (from the conclusion of chapter 6). Based on these data, a two layer model, which divides the oxide layer into an outer layer (thickness = t_1) and an inner layer (thickness = t_2), can be used to determine the thickness of oxide formed on NiCr surface. The model is illustrated in Fig 8-4 in which for simplification the small amount of NiO in t_2 layer is neglected. The mean escape depths for Cr(2p) and Ni(2p) photoelectrons in the oxide layer are estimated to be 9 ML and 7 ML.

Fig. 8-3 Ni(2p) and Cr(2p) XPS spectra of an oxidized (300 L) NiCr alloy after sputtered by 4 keV, 1.5 μA Ar^+ for 1 minute.

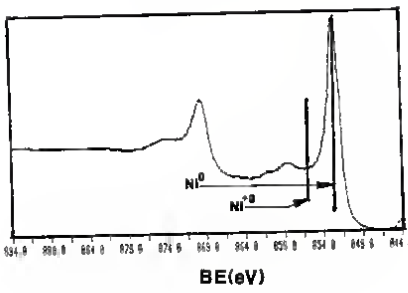
Ni0
Ni+2
BE(eV)

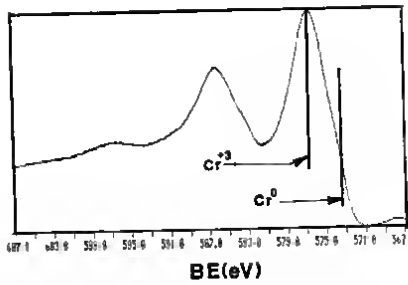
Cr+3
Cr0
BE(eV)

Fig. 8-4 A two-layer model for oxide formed on NiCr alloy after 300 L O_2 exposure.

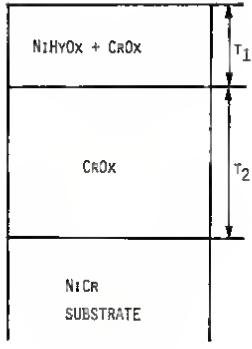
NiHyOx + CrOx
T_1
CrOx
T_2
NiCr
SUBSTRATE

respectively [93].

According to the model the XPS Ni(2p) intensity of Ni hydroxide (Nihyox) from outer layer can be written as

$$I_{Nihyox}(\theta) = K_{Ni}(\theta) \cdot \sigma_{Ni} \cdot \sigma_{Nihyox} \cdot \int_0^{t1} C_{Nihyox}(x) \cdot \exp[-x/(\Omega_{Ni}\sin\theta)]\, dx, \qquad [8\text{-}1]$$

and the intensity of metallic Ni (Ni) from substrate as

$$I_{Ni}(\theta) = K_{Ni}(\theta) \cdot \sigma_{Ni} \cdot \int_{(t1+t2)}^{\infty} C_{Ni}(x) \cdot \exp[-x/(\Omega_{Ni}\sin\theta)]\, dx, \qquad [8\text{-}2]$$

where K_{Ni} is a combined response function of analyzer and excitation flux, σ_{Ni} is the photoionization cross section, σ_{Nihyox} is the coverage of Ni hydroxide on the outer oxide layer, Ω_{Ni} is the mean escape depth of Ni(2p) photoelectron in oxide (assumed constant for hydroxide and all oxides), and $C_{Ni}(x)$ and $C_{Nihyox}(x)$ are the depth composition functions of metallic Ni and Ni hydroxide, respectively. The exponential term represents the attenuation of flux contribution from depth x.

Assuming the depth composition functions $C_{Ni}(x)$ and $C_{Nihyox}(x)$ are constants, $I_{Nihyox}(\theta)$ and $I_{Ni}(\theta)$ can be reduced to

$$I_{Nihyox}(\theta) = K_{Ni}(\theta) \cdot \sigma_{Ni} \cdot a_{Nihyox} \cdot C_{Nihyox} \cdot \Omega_{Ni} \cdot \sin\theta \cdot [1-\exp[-t_1/(\Omega_{Ni}\sin\theta)]], \quad [8-3]$$

$$I_{Ni}(\theta) = K_{Ni}(\theta) \cdot \sigma_{Ni} \cdot C_{Ni} \cdot \Omega_{Ni} \cdot \sin\theta \cdot \exp[-(t_1+t_2)/(\Omega_{Ni}\sin\theta)]. \quad [8-4]$$

For the case of an 80%Ni-20%Cr alloy, even if the substrate layer next to inner oxide is completely depleted of Cr, there is only a 20% maximum error for assuming constant composition of metallic Ni. Therefore, the assumption of constant metallic Ni composition, C_{Ni}, in the substrate is reasonable. This is also the reason for choosing Ni signal rather than using Cr signal to calculate the thickness of oxide, since Cr composition can be changed more drastically after oxidation compared to Ni.

Taking the ratio $R(\theta)$ of $I_{Nihyox}(\theta)$ and $I_{Ni}(\theta)$, the pre-exponential terms such as $K_{Ni}(\theta)$, σ_{Ni}, Ω_{Ni} and $\sin\theta$ are cancelled and $R(\theta)$ is written as

$$R(\theta) = \frac{I_{Nihyox}(\theta)}{I_{Ni}(\theta)} = \frac{(a_{Nihyox}) \cdot (C_{Nihyox})}{(C_{Ni})} \cdot \frac{[1-\exp[-t_1/(\Omega_{Ni}\sin\theta)]]}{[\exp[-(t_1+t_2)/(\Omega_{Ni}\sin\theta)]]}, \quad [8-5]$$

Dividing $R(\theta)$ by $R(85°)$, the parameters like σ_{Ni}, C_{Nihyox} and C_{Ni} are further cancelled, and the resultant equation, $A(\theta)$, is

written as

$$A(\theta) = \frac{R(\theta)}{R(85^\circ)} = \frac{[1-\exp[-t_1/(\Omega_{Ni}\sin\theta)]] \cdot \exp-(t_1+t_2)/(\Omega_{Ni}\sin 5^\circ)}{[1-\exp[-t_1/(\Omega_{Ni}\sin 85^\circ)]] \cdot \exp-(t_1+t_2)/(\Omega_{Ni}\sin\theta)} \qquad [8-6]$$

$A(\theta)$ is a function of t_1, t_2 and θ alone.

The peak area of Ni hydroxide on NiCr is only ~20% of that of NiO on pure Ni at 45° take-off angle. By using equation [8-7]

$$I_{Niox} = I^{\infty}_{Niox} \cdot [1 - \exp[-t/(\Omega_{Ni}\sin\theta)]] \qquad [8-7]$$

and assuming 3 ML of NiO on pure Ni the thickness of Ni hydroxide t_1 is calculated to be 0.5 ML. The thickness of Ni hydroxide also can be estimated from Ar^+ sputtering. According to the condition of sputtering t_1 was estimated to be ~1 ML (94).

Setting t_1 = 1 ML, the calculated $A(\theta)$ curves for t_2 = 1 ML to 4 ML as well as the experimental $A(\theta)$ ratios are shown in Fig.8-5. The experimental $A(\theta)$'s fit the calculated curve of t_2 = 4 ML very well at take-off angle ≥45° but the experimental $A(\theta)$ values gradually deviated from this towards the curves of smaller t_2 values as take-off angle decreased. It is known that at lower take-off angles some factors like surface roughness tend to complicate the results of ARXPS (95,96). Since the t_2 value is consistently fitted to 4 ML at higher take-off angle i.e. $\theta \geq 45^\circ$, it is reasonable to conclude t_1 = 1 ML and t_2 = 4 ML from the present model.

Fig. 8-5 Experimental A(θ) (see text) versus take-off angle. The dashed lines are calculated based on equation 8-6 in the text where t_1 = 1 ML

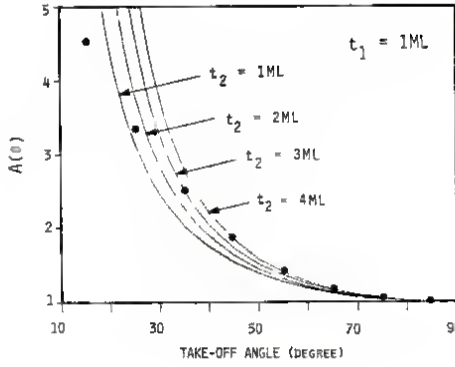
t_1 = 1ML
t_2 = 1ML
t_2 = 2ML
t_2 = 3ML
t_2 = 4ML
A(0)
TAKE-OFF ANGLE (DEGREE)
1
2
3
4
5
10
30
50
70
90

Segregation of Cr

The line shapes and the binding energies of XPS Cr(2p) spectra of Cr_2O_3 from oxidized NiCr alloy are the same as those from oxidized pure Cr indicating that the initially dispersed Cr atoms in the alloy aggregated to form three dimensional Cr oxide. Due to the lower density of Cr atoms in NiCr substrate than in Cr_2O_3, the formation of 3-D Cr oxide may require the depletion of Cr atoms from neighboring areas and from deeper layer if the amount of Cr oxide is large enough. Using the bulk density (Cr_2O_3 = 5.21 g/cm^3 and Ni = 8.9 g/cm^3), it needs to deplete all the Cr atoms from 9 layers of Ni-20%Cr alloy to form 4 complete Cr_2O_3 layers on the surface. Since the amount of Ni hydroxide formed is quite small in the present case oxidation of Cr atoms produces extra metallic Ni in the t_2 layer and/or below oxide layer depending the amount of Cr_2O_3 formed in t_2 layer. This phenomenon is confirmed by the results of metallic Cr to Ni ratio as shown in Fig 8-2.

The deviation of experimental $A(\theta)$ values from the calculated curves at lower take-off angle in Fig 8.5 could be explained by the presence of metallic Ni in the inner oxide (t_2) layer. At lower take-off angles, contribution of any metallic Ni from the t_2 layer would become more important, and would reduce the $A(\theta)$ ratios. For the present case t_1 = 1 ML and t_2 = 4 ML, if we assume 20% of metallic Ni is in the t_2 layer, the intensity of metallic Ni from t_2 layer is

calculated to be 165 % of that from 80%Ni-20%Cr substrate at 15° take-off angle. This percentage is reduced very quickly as take-off angle increases, and the percentage is reduced to 25% and 20% at θ=45° and 55°, respectively.

If the effect of surface roughness is small, the percentage of metallic Ni in t_2 layer should be able to be obtained from equation [5-4] and [5-9]. Consider the existence of metallic Ni in the t_2 layer, equations [5-5] and [5-6] can be re-written as

$$R(\theta) = \frac{I_{Nihyox}(\theta)}{I_{substrate}(\theta) + I_{Ni}t2(\theta)} = \frac{(m_{Nihyox}) \cdot (C_{Nihyox})}{(C_{Ni})} \cdot$$

$$[1-\exp[-t_1/(\Omega_{Ni}\sin\theta)]] \cdot 1/[\exp[-(t_1+t_2)/(\Omega_{Ni}\sin\theta)]$$

$$+ r\cdot\exp[-t_1/(\Omega_{Ni}\cdot\sin\theta)] * [1-\exp[t_1/(\Omega_{Ni}\cdot\sin\theta)]]], \qquad [5-8]$$

and $A'(\theta) = R'(\theta)/R(45°)$. [5-9]

However, the experimental data can not satisfactorily fit equation [5-9] particularly at 15°, suggesting the surface roughness effects can not be neglected. It is not surprising to find a rough NiCr oxide surface, since our sample is a polycrystalline crystal, and the first monolayer of oxidized NiCr surface is consisted of at least two compounds (Ni hydroxide and Cr oxide) and four elements (Ni, Cr, O and H).

As a result of the formation of the oxide layer, the metallic Cr signal from the substrate is attenuated. After 300 L of oxygen, the

metallic Cr peak in the NiCr spectrum is hardly detectable, while a large metallic Cr peak is seen from pure Cr (fig 8-6). The much larger extension of attenuation of the Cr metallic peak from NiCr as compared to pure Cr intuitively suggests that the oxide layer formed on NiCr alloy is perhaps much thicker than that on pure Cr. Using the attenuation intensity equation for a homogeneous overlayer:

$$I_{Cr} = I^{\infty}_{Cr} \cdot \exp[-t/(\Omega_{Cr} \sin\theta)]. \qquad [8\text{-}10]$$

the thickness t of the Cr oxide layer on pure Cr is calculated to be 5.6 ML. Previously reported showed 4 ML on a similar sputtered polycrystalline pure Cr sample [97], similar to the 4 ML of Cr_2O_3 on NiCr surface reported above. These calculated oxide thicknesses show that the above intuitive explanation for the observation of a small metallic Cr peak from oxidized NiCr Cr(2p) spectrum is wrong. Rather the lack of this peak must be explained by the existence of a depleted metallic Cr region (or Ni rich region) due to segregation of Cr atoms from deeper layer to surface reaction product. The thickness of the Cr depleted layer can be estimated by directly substituting the peak areas of metallic Cr(2p) of clean and oxidized NiCr alloy into equation [8-10], and a thickness of ~11 ML is calculated for the depleted layer. Considering the 5 ML oxide layer (Ni hydroxide + Cr oxide), the metallic Cr depleted layer is estimated to be 6 ML thick as compared to 9 ML estimated by conservation of atoms.

The model for NiCr oxide layer deduced from ARXPS results is

Fig. 2-6 Cr(2p) XPS spectra at $\theta = 45°$ for NiCr alloy and pure Cr exposed to 300 L O_2

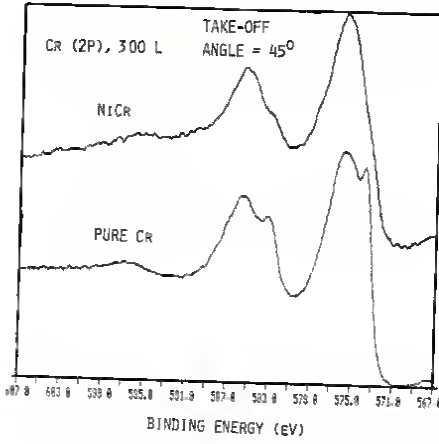
CR (2P), 300 L
TAKE-OFF
ANGLE = 45°
NiCR
PURE CR
587.0
583.0
579.0
575.0
571.0
567.0
BINDING ENERGY (eV)

depicted in Fig 8-7. As it shown, the outer layer (1 ML thick) is a mixture of Ni hydroxide and Cr oxide; the inner oxide layer (4 ML thick) is mostly Cr oxide with small amount of NiO (which was concluded from chapter 6 and neglected in the above analyses) and possibly some metallic Ni, and finally a 6 ML thick metallic Cr depleted (Ni rich) layer exists above NiCr base substrate. The submonolayer Ni hydroxide is confined in the outer oxide layer, which probably resulting from preferential oxidation of Cr at early oxygen exposures. Since after Cr oxide is formed, only limited amount of Ni remains in the surface region. In addition, the presence of ~6 ML thick metallic Cr depleted layer suggests the mobilities of Cr atoms and/or O atoms are not as small as expected at room temperature. The high atomic mobilities probably are provided by the large heat released during the formation of Cr oxide.

Comparison With Previous Results

It is interesting to compare the present results with those obtained by other methods. The AES sputter profile of oxidized NiCr shown in Fig 8-8(a) has been quantified by Saez and Hofmann (94) using a sequential layer sputtering model. The composition of the oxide film was deduced as shown in Fig 8-8(b) (redrawn from (94)). Consistent with the present study, the outer monolayer was concluded to be a mixture of NiO and Cr_2O_3, while the inner oxide layer was concluded to be three monolayers of Cr_2O_3 for a total thickness of 4

monolayers, which is slightly different from the present ARXPS study. The other differences are the metallic Ni in the Cr_2O_3 layer and the Cr depleted region in substrate as detected by ARXPS. In general the bilayer nature of the oxide is confirmed by both approaches.

Summary

In summary, the oxide structure of NiCr alloy after 300 L oxygen exposure was studied mainly by ARXPS. As shown in Fig 5-4, a complicated model for the oxide structure was established. The outer one monolayer oxide layer is a mixture of Ni hydroxide and Cr oxide and the inner four monolayer oxide layer consisted of Cr_2O_3, metallic Ni and small amount of NiO. In addition, a layer having extra metallic Ni (depleted of Cr) may exist in the substrate region next to the oxide layer. In contrast to the three monolayer NiO formed on the pure Ni surface, the limited formation of Ni hydroxide in the first oxide monolayer clearly demonstrates the increase of passivation of the Ni substrate by the addition of Cr.

Fig. 8-7 Schematic of the model derived from angle-resolved XPS analysis for the surface of NiCr alloy exposed to 300 L O_2 at room temperature

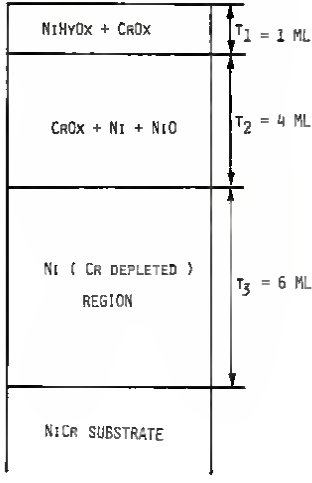
NiHyOx + CrOx
T1 = 1 ML
CrOx + Ni + NiO
T2 = 4 ML
Ni (Cr DEPLETED)
REGION
T3 = 6 ML
NiCr SUBSTRATE

Fig. 8-8 Sequential sputter model (above). Auger peak intensities versus sputter time for Ni-20%Cr alloy exposed to 400 L O_2 at room temperature (below). Quantitative analysis of the sputter profile shown in Fig. 8-7 (above) (see text for explanation). (Fig. 8-7 (above) reprinted from ref96 with permission)

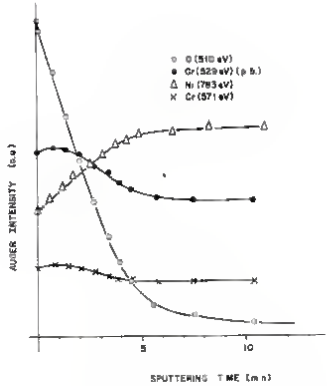
O (510 eV)
Cr (529 eV) (p.b.)
Ni (783 eV)
Cr (571 eV)
AUGER INTENSITY (a.u.)
5
10
SPUTTERING TIME (mn)

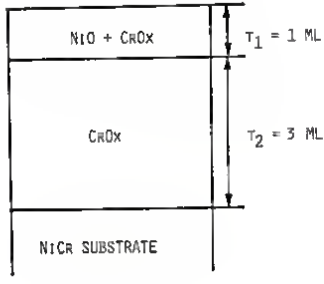
NiO + CrOx
CrOx
NiCr SUBSTRATE
T1 = 1 ML
T2 = 3 ML

CHAPTER 9
ELECTRON STIMULATED ION DESORPTION (ESID)

Electron Stimulated Ion Desorption (ESID) experiments were performed because of the ability and sensitivity of the technique to detect hydrogen and hydrogen containing species at solid surfaces (98,99,100)

Results

The ions desorbed from the surfaces of Ni(110) and NiCr(110) after 300 L oxygen exposures are shown in Fig 9-1, where ion yields are plotted with a linear scale. Ion species such as $^{1}H^{+}$ $^{16}O^{+}$ $^{17}OH^{+}$ and $^{19}F^{+}$ (or H_3O^{+}) etc, were desorbed from oxidized Ni(110) surfaces As compared to Ni(110), the ESID spectrum of NiCr(110) had a much larger O^{+} emission and a negligible OH^{+} emission. The intensities of H^{+} emission from both surfaces were roughly equal. F^{+} ion is a common contaminant ion observed in ESID experiments due to its large (10^{-16} - 10^{-18} cm^{2}) desorption cross section (101). Despite the relatively large F^{+} signal, the real fluorine concentration at surface was probably very small (undetected by AES or XPS)

The H^{+} and OH^{+} emissions from Ni(110) and NiCr(110) surfaces were monitored in-situ during oxygen exposure. The ion yields as a function of oxygen exposure are depicted in Fig 9-2. The OH^{+} signal is normalized to the H^{+} signal at 200 L. The H^{+} emission curve from

Fig. 9-1 ESD mass spectra for Ni(110) and NiCr(110) exposed to 300 L O_2 at room temperature.

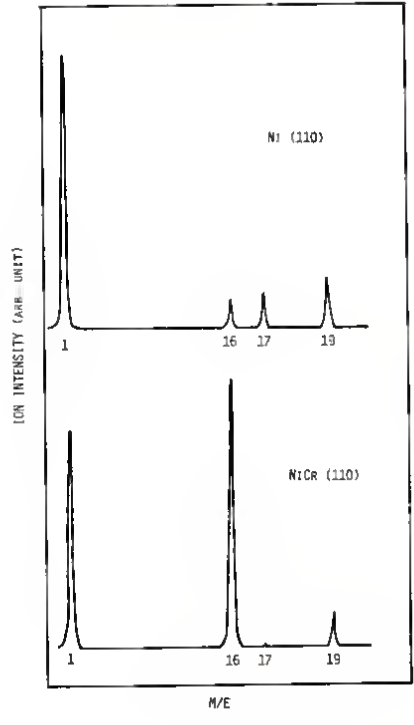
Ni (110)
1
16
17
19
NiCr (110)
1
16
17
19
ION INTENSITY (ARB. UNIT)
M/E

Fig 9-2 ESD H⁺ and OH⁺ intensities and XPS OH O(1s) peak area versus oxygen exposure for Ni(110) and NiCr(110)

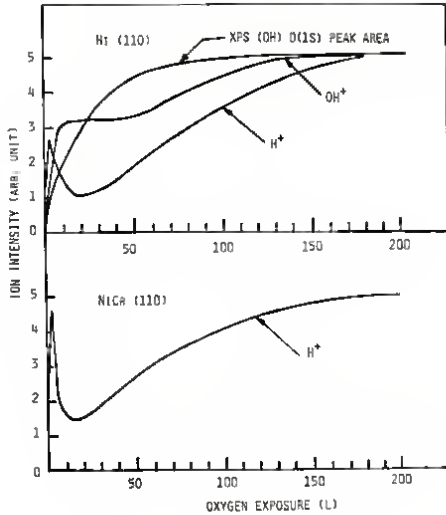
Ni (110)
XPS (OH) O(1S) PEAK AREA
OH+
H+
NiCr (110)
H+
ION INTENSITY (ARB. UNIT)
OXYGEN EXPOSURE (L)
0
1
2
3
4
5
50
100
150
200

pure Ni surface can be divided into three stages. Following a initial rapid increase of H^+ intensity in the first .1 L of oxygen exposure the H^+ intensity decreased continuously until oxide nucleated on the surface at 20 L then H^+ signal kept rising with further oxygen exposure. H^+ signal did not reach a saturation value and still showed a slow increase even after oxide passivated the surface at .120 L. The second increase of H^+ emission from the Ni surface starting at .20 L seems to be associated with the nucleation and growth of Ni oxide. Similar H^+ emission curve was also observed during exposing NiCr surface to oxygen. Perhaps because the oxidation reaction occurred more rapidly on NiCr, the onset of the second increase of H^+ emission from NiCr surface shifted toward lower oxygen exposure as compared to that of Ni.

The OH^+ emission from the Ni surface can also be divided into three stages. A rapid increase of signal was observed in the first 5 L. After that the OH^+ signal remained relatively constant for oxygen exposures between 10 to 50 L, unlike the drastic changes of H^+ emission. At oxygen exposures above 50 L OH^+ signal rose again and finally reached a saturation value at .120 L of oxygen exposure. The OH^+ signal from NiCr was very small, and consequently no signal was monitored during oxygen exposure.

Desorption of O^+

Knotek and Feibelman (KF) (102) have proposed a model of ESID, which is based on the Auger decay of core hole created by electron

impact. For transition metal oxide, TiO_2, they have shown experimentally that the desorption of O^+ from the surface is initiated by creation of a Ti 3p core hole followed by an Auger decay process. Since the Ti valence electrons are completely transferred to the O in TiO_2 (Ti^{+4} is in a noble gas configuration) the dominant deexcitation process is an interatomic Auger transition which removes 2 or 3 electrons from an O^{-2} ion. The resultant positive ions of Ti^{+4} and O^+ repels one another coulombically resulting in an electron desorption of O^+ ions. As a result, the so called maximal-valency compounds such as TiO_2, V_2O_5 and WO_3 are expected to have strong desorption of oxygen. On the other hand, submaximal-valency compounds, that is, compounds in which the metal atom is not ionized to the noble gas configuration like NiO and $Cr2O_3$, are expected to show much smaller O^+ yield than maximal-valency oxides since the interatomic Auger transition is no longer the dominant deexcitation process. Unlike KF model, the other ESID models like Menzel-Gomer-Redhead (MGR) model [103,104] do not adequately explain how an O^{-2} ion loses 3 electrons to desorb as an O^+ ion and why a threshold in the O^+ ion yield appears at a primary beam energy which excites the Ti 3p level even though it is not directly involved in bonding.

Desorptions of oxygen from NiO and Cr_2O_3 compounds are not favored by the model of Knotek and Feibelman, but substantial O^+ desorptions have been observed experimentally on room temperature oxidized Ni (105-109) and Cr (106,110-117) surfaces. Though KF model

agreed well with the data from nearly defect-free single crystal oxides (102), those experimental results suggest that KF model is not the only de-excitation channel for the desorption of oxygen from metal surfaces oxidized at room temperature and other types of excitation and decay processes may be responsible for. For example, Verhoeven and co-workers (108) suggested that the desorption of positive oxygen ions from room temperature oxidized Ni surface can be resulted from multiple excitations in which the O 2s inner shell is involved. Dawson and co-workers (110) also found O^+ desorption from oxidized Cr surfaces with primary electrons whose energies were near the O 2s core level rather than Cr 3p core level suggested by KF model.

In conjunction with the chemical information obtained by ARXPS results, the ISS data indicates that both Ni hydroxide and Cr oxide were present on the oxidized NiCr surface. Because of the high re-neutralization probabilities for the ions produced in the sub-surface, the low-energy ions emitted by ESID are expected to originate only from the top monolayer of the surface, similar to ISS (98,100). Therefore, the Cr_2O_3 and Ni hydroxide on the oxidized NiCr surface could both be responsible for the O^+ desorption signal. No ESID results were ever reported on Ni hydroxide, but strong O^+ emission from Cr surface oxidized at room temperature has been reported (104,110-117). It is impossible to conclude which compound is the source of strong O^+ emission from the present data. Possible

further work would be to measure threshold energies or energy analysis of desorbing ions.

Desorption of H^+ and OH^+

Oxidized NiCr surface had a much smaller $(OH)^+$ emission than oxidized Ni surface. Because XPS O(1s) spectra did not show such large difference in the amount of (OH) on oxidized Ni and NiCr, the possibility of different (OH) desorption signals due to the population of (OH) species at Ni and NiCr surfaces can be excluded. It is necessary to explain the difference in the (OH) ion yields in terms of the different bonding conditions and arrangements of hydroxyl groups between the two surfaces.

Model for Desorption of H^+ and OH^+

A. Desorption of OH^+

Knotek and co-workers (102,119-121) have studied in detail the OH^+ and H^+ desorptions from adsorbed surface (OH) groups on TiO_2, where OH^- adsorbs at surface Ti ion site via its O atom. By measuring ion yields as a function of incident electron energy, they found that the threshold energy for desorption of OH^+ coincides with the O(2s) core level. They pointed out that since the adsorbed (OH) exist in a -1 charge state rather than the -2 state of O in TiO_2, the change to $(OH)^{+1}$ requires the transfer of only two electrons. Therefore an O(2s) core hole followed by an intratomic Auger decay

can yield an OH^+ ion for desorption. This is different from the desorption of O^+ ion which requires removal of three electrons by creation of a Ti(3p) core hole and followed by an interatomic Auger decay. Knotek [121] further reported that the major threshold energy for H^+ in the presence of adsorbed (OH) is also at the O(2s) level. Knotek explained that the yield of H^+ from O-H depends upon the stability of the bond between O and H. Decay of an O(2s) level can either fragment the OH by removing two electrons from the σ-orbital yielding an H^+ desorption, or remove two electrons from orbitals other than the σ-orbitals yielding a stable OH^+ desorption. It is noteworthy that the metal atom is not involved in Knotek's model for the desorptions of OH^+ and H^+ from adsorbed surface OH group and the ESID of H^+ and OH^+ from adsorbed OH are determined only by O-H bond itself. Consequently, Knotek's model may also be applicable to the Ni and NiCr surfaces.

B. Desorption of H^+

For TiO_2 not all the H^+ are desorbed from adsorbed surface hydroxyl. Knotek found that H^+ can also be desorbed from the hydrogen bonded to surface Ti [120,121]. This Ti - H hydride type bond was also deduced from a combined XPS, EELS, TDS, electron paramagnetic resonance, surface conductivity and work function measurement studies by Gopel et al. on TiO_2 (110) [122]. In addition, from both ESID and photon-stimulated ion desorption (PSID) results [119-121], Knotek found that hydrogen can be bonded to a subsurface (or bridge-

bonded) oxygen in a hydroxyl-like bond. The creation of an O(2s) hole will cause desorption of a H^+ but not an OH^+.

In-situ Measurement of H^+ and OH^+ on Pure Ni(110)

The change of H^+ yield as a function of oxygen exposure similar to that study is commonly observed during oxidation of other metals.* The major residual gas in the UHV chamber at 10^{-10} Torr range was hydrogen. After the sputter/clean procedure, during cooling the annealed Ni surface was exposed to ~ 0.3 L of hydrogen at 300 °K, and a substantial amount of hydrogen could adsorb on the "clean" annealed Ni surface and form H - Ni bond. Because only an extremely small H^+ signal was observed from a hydrogen dosed surface before any surface oxygen could be detected by AES, the emission of H^+ is definitely associated to the presence of surface oxygen in agreement with the conclusions of other authors (123-128).

For the first ~1 L of oxygen exposure, the fast increase in H^+ emission could be mainly from H-Ni bond. The increased yield of H^+ from H-Ni bond may be due to the weakened H-Ni bonds through an interaction between O and Ni (127) or the decreased neutralization effect. The subsequent decrease followed by an increase of the H^+ signal with further oxygen exposure can be a net results of displacement of adsorbed H by O and the increase of OH bonds. It is interesting to note that Bennighoven and co-workers (130) found an

* T.E. Madey, private communication.

increase followed by a decrease of Ni^{+}/Ni^{+} and Ni_2H^{+}/Ni_2^{+} SIMS intensity ratios (these ratios are known to represent the amount of Ni-bonded hydrogen) upon exposing Ni to O_2. The decreases of the ratios NiH^{+}/Ni^{+} and Ni_2H^{+}/Ni_2^{+} indicate a decreasing concentration of metal bonded hydrogen. It is believed that similar interactions between oxygen and hydrogen covered Ni surface caused the changes of the ESID H^{+} and the SIMS NiH^{+}/Ni^{+} as well as Ni_2H^{+}/Ni_2^{+} ion ratios.

The OH XPS O(1s) peak area as a function of oxygen exposure is also depicted in Fig.9-2(a). The OH O(1s) uptake curve generally agrees with OH^{+} emission curve, suggesting that the majority of OH on the Ni surface is indeed adsorbed surface hydroxyl (similar to the conclusions derived in chapter 6) since subsurface hydroxyl can not yield OH^{+}. Anderson et al. (132) also found adsorbed hydroxyl on the Ni oxide surface after exposing the clean Ni(100) to 300 L of oxygen at room temperature by electron energy loss spectroscopy (EELS). However the more drastic changes in H^{+} emission curve again suggests that H^{+} can be desorbed from some species other than surface hydroxyl. After nucleation of NiO, both H^{+} and OH^{+} signals were increased simultaneously with the increase of oxygen exposure indicating that adsorbed surface OH is not H-Ni, is the major source for H^{+}.

Arrangements of (OH) on Ni and NiCr surfaces

A substantial amount OH^{+} was desorbed from pure Ni surface. As suggested by ARXPS results in chapter 6, (OH) species only adsorbed

at oxidized pure Ni surface in agreement with the ESID results. The adsorbed (OH) probably is bound in the first monolayer of Ni oxide via the oxygen atom, with the hydrogen atom pointing away from the surface (123-126,128). The adsorbed (OH) may have a polar angle (measured with respect to the surface normal) less than 60°, since strongly inclined OH bonds do not yield H^+ (128).

Only negligible amount of OH^+ was desorbed from oxidized NiCr surface. However XPS O(1s) spectra indicated substantial amount of hydroxyl species on the surface. To explain the discrepancy it is reasonable to propose that either the hydroxyl species are strongly inclined having a very large polar angle on NiCr surface or hydrogen is bonded to subsurface (or bridge-bonded) O in a hydroxyl like bond. Since strongly inclined surface O - H can not yield either OH^+ or H^+, the large H^+ emission from oxidized NiCr surface then suggests that H-subsurface (or bridge-bonded) oxygen bonds are likely present on NiCr surface. Ni hydroxide was found on NiCr surface after 300 L oxygen exposure (see chapter 5). Because no surface structure and arrangement of (OH) groups on Ni hydroxide were ever reported in the literatures and the formula for Ni hydroxide can be potentially complicated**, the presence of hydroxyl like bonds, such as H-subsurface (or bridge-bonded) O and strongly inclined surface O-H perhaps provides a picture for the surface structure of Ni hydroxide formed on NiCr surface.

** At least four types of Ni hydroxide ($Ni(OH)_2$ and α-$NiO(OH)$, β-$NiO(OH)$ and γ-$NiO(OH)$) can be formed. These hydroxides have nearly identical Ni(2p) and O(1s) XPS spectra [82,133], it is not possible to distinguish these species using XPS alone.

Summary

In summary, it has been found that adsorbed (OH) exists on the surface of oxidized Ni surface, and Ni hydroxide exists on the oxidized NiCr surface (chapter 6). The ESID results support the existence of (OH) groups on both surfaces. The different H^+ and OH^+ desorptions behaviors on oxidized Ni and NiCr surfaces may be understood in terms of the different (OH) and H bonds on the surfaces.

CHAPTER 10
FORMATION OF (OH) SPECIES

Introduction

It is important to recognize the existence of (OH) species on the oxidized Ni surface during oxygen exposure. As discussed previously, because of the controversy about the assignment of high B.E. O(1s) peak and/or inefficient analysis of oxygen gas purity the existence of (OH) species has been ignored by most authors studied the oxidation of Ni. However, few authors have noticed the presence of (OH) species on the Ni surface during oxygen exposure in the UHV chamber [68,75,134,135].

For example, Bourgeois and Pardreau [134,135] have studied the formation of hydroxyl species on Ni(100) and (110) by static SIMS. Different hydrogen-containing cluster ions, which were correlated to the extent of the oxidation reaction and formation of hydroxyl species, have been observed. The conclusions from their studies are as followings: (1) During the oxygen chemisorption stage, the most intense hydrogen containing ionic intensity was $NiOH^+$. Both Ni_2H^+ and Ni_2OH^+ were also present but less intense, and NiO^+ was not observed. (2) after the nucleation of NiO oxide, $NiOH^+$ was not observed any more, but Ni_2H^+ and Ni_2OH^+ were still observed. Moreover, negative

hydrogen-containing cluster ions, like OH^-, O_2H^- and Ni_2H^-, appeared. Boutgeois and Perdereau's results provide direct evidence for the formation of hydroxyl species at Ni surface during oxygen exposure.

Sources for the Formation of (OH)

Results

Several different species, such as the hydrogen and water in the UHV chamber and subsurface hydrogen either implanted during sputter cleaning procedure or incorporated during sample preparation, can be responsible for the formation of hydroxyl species during oxygen exposure. To find out which species is responsible for the formation of hydroxyl, (1) an annealed Ni(110) surface was exposed to 300 L of 50% oxygen - 50% water mixture at a total pressure of 1×10^{-7} Torr at room temperature, and (2) a sputter cleaned (not annealed) Ni(110) surface was exposed to 300 L of oxygen at 5×10^{-8} Torr*.

* Because background hydrogen was increased dramatically as a result of admitting Ar to the UHV system, a mixture of argon and hydrogen was implanted into Ni during sputter cleaning procedure. Due to smaller mass, the penetration depth of hydrogen is much larger than Ar. As a result, a substantial amount of hydrogen could be retained in the substrate after sputtering.

The O(1s) spectra after 300 L of oxygen and oxygen - water mixture exposure are compared in Fig.10-1. The hydroxyl component of O(1s) spectrum is larger for water - oxygen mixture exposed surface than for oxygen exposed surface indicating the amount of surface hydroxyl species was affected by the partial pressure of water. However, it was noticed that other impurity gases were also present with water and oxygen, particularly hydrogen was in a substantial amount.

The O(1s) spectra of both Ar^+ sputtered and annealed Ni(110) after 300 L of oxygen exposure are compared in Fig 10-2. The high B.E. O(1s) peak for the sputtered surface is twice or large as that for the annealed surface. This suggests that sputtering could have important effects on the formation of hydroxyl species.

Discussion

Four possible sources for the formation of hydroxyl species are considered, namely the hydrogen and water in the UHV chamber and the subsurface hydrogen either implanted during sputter cleaning procedure or incorporated during sample preparation.

A. UHV Hydrogen

According to the RGA analyses in chapter 2, hydrogen is the most abundant residual gas (59.2%), while water is only in minor amount (0.54%). Because of the large amount of (OH) on the oxidized Ni surface (about 20% of the total O(1s) area at 45° take-off angle)

Fig. 10-1 O(1s) spectra at $\theta = 15°$ for Ni(110) (a) exposed to 300 L O_2 at $P_{O2} = 5 \times 10^{-8}$ Torr and (b) exposed to 300 L ($O_2 + H_2O$) at $P_{O2} = P_{H_2O} = 5 \times 10^{-8}$ Torr.

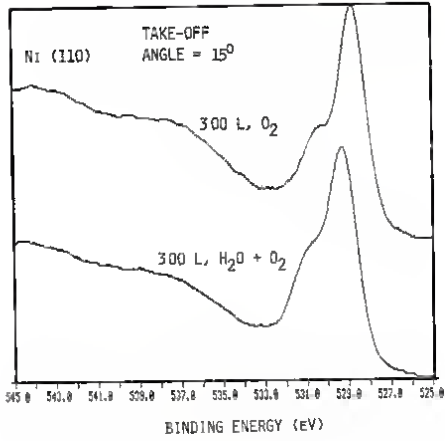
TAKE-OFF
ANGLE = 15°
Ni (110)
300 L, O2
300 L, H2O + O2
545.0
543.0
541.0
539.0
537.0
535.0
533.0
531.0
529.0
527.0
525.0
BINDING ENERGY (eV)

Fig 10-2 O(1s) XPS spectra at $\theta = 45°$ for (a) sputtered unannealed and (b) well annealed Ni(110) both exposed to 300 L O_2 at 5×10^{-8} Torr.

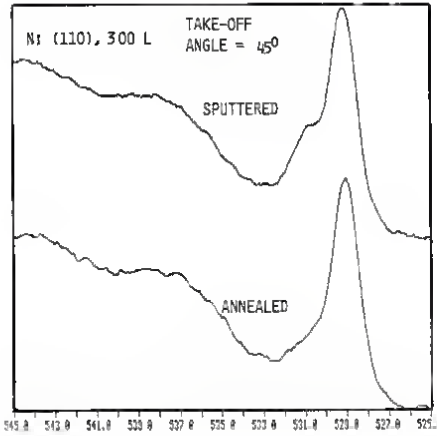
N: (110), 300 L
TAKE-OFF
ANGLE = 45°
SPUTTERED
ANNEALED
545.0 543.0 541.0 539.0 537.0 535.0 533.0 531.0 529.0 527.0 525.0
BINDING ENERGY (EV)

water apparently can not be the major source for formation of (OH) in the present case. After examining other hydrogen containing gases like CH_4, hydrogen appears to be a most possible source for (OH) formation simply because of its large impingement rate and reactivity.

Benninghoven et al [136] have used static SIMS to study the interactions between oxygen and hydrogen on an annealed polycrystalline Ni surface at room temperature. They found that oxygen exposure of a hydrogen covered surface only result in a removal of the hydrogen adsorption layer accompanied by the usual oxygen incorporation into the surface. On the other hand, hydrogen exposure of nickel surfaces covered by various amounts of oxygen results in the formation of OH groups on the surface.

To simulate the experiments of Benninghoven et al., Ni surfaces were exposed to 50 L of hydrogen after 1 L (chemisorption region) and 300 L (NiO covered surface) of oxygen exposure, respectively. No other treatments like heating were applied to the pre-oxygen dosed surfaces. It was found the O(1s) peak areas of the (OH) species already present on the surface after oxygen exposures were not affected by the subsequent hydrogen exposure. These results do not resemble the results reported by Benninghoven, which showed that the amount of hydroxyl can be increased by hydrogen exposure. However, the discrepancy may be explained by the very small amount of (OH) on the starting oxidized Ni surface used in the experiments of Benninghoven et al. (judged from the very low $(OH)^-$ secondary ion

intensity before hydrogen exposure), and their "clean" (containing less hydroxyl) oxidized Ni could be more reactive to hydrogen than the hydroxyl covered oxidized surface.

Though exposure of hydrogen alone has negligible effect on the amount of (OH) already present on the oxidized surface in the present study, the intensity of ESID OH^+ signal and XPS O(1s) high K.E. peak on Ni(110) were continuously increased even after the entire surface was covered by NiO at an oxygen exposure ≥ 50L as shown in Fig. 9-2. In the present study, the oxygen exposure is really a mixture exposure of oxygen and hydrogen ($P_{O2} : P_{H2} = 3 : 1$). This suggests that mixtures of hydrogen and oxygen gases are essential to the continuous formation of (OH) during oxygen exposure.

B. UHV Water

Besides hydrogen gas, water usually is one of the major hydrogen containing residual gas in the most of UHV chambers. It is known that water alone has a very low sticking coefficient to both clean Ni and NiO of low surface defect density at room temperature. However, it was reported that the dissociation of H_2O on clean Ni(110) can be promoted by surface oxygen (137-141), and can also be enhanced by "neo-lattice" oxygen on defective NiO (142,143).

Hydroxyl species can be produced by the adsorption of H_2O on oxygen pre-dosed Ni surface through the reaction (144)

$$H_2O_{gas} + 1/2\ O_{adm} \rightarrow 2(OH)_{ads}$$

which indicates one dissociated water molecule produces two identical adsorbed (OH). Benndorf et al. (139) showed that both clean (θ_O = 0 ML) and heavily oxidized ($\theta_O \geq 0.65$ ML) Ni(110) surfaces are inert to water adsorption at room temperature.** However, some water adsorbs and decomposes when the oxygen coverage is in a critical intermediate range ($0 < \theta_O < 0.65$ ML) on clean Ni. Therefore, if oxidized Ni is exposed to water alone the reaction, $H_2O_{gas} + 1/2\ O_{ads} \rightarrow 2(OH)_{ads}$ will be applicable only to the chemisorption stage. Complementary to the work of Benndorf et al., McKay et al. (142,143) have found that extra Ni cations and non-lattice oxygen in the surface region as promoters are essential for the dissociation of water on NiO(100). It was proposed that the non-lattice oxygen facilitates the abstraction of hydrogen from water and the defect site (oxygen vacancy) next to Ni cation accommodates the resultant (OH) fragment. From McKay's work the results of Benndorf et al. can be explained by the lack of free Ni cation on heavily oxidized Ni surface, or the increase of geometrical site-blocking resulting from the dissociation of water (144).

** Prior to Benndorf's water adsorption experiment (139), the pre-adsorbed oxygen was annealed at 550°C which probably removed the adsorbed surface (OH) introduced during oxygen exposure, and also produced more ordered surface oxygen structures.

However, the results of mixture exposure of water and oxygen can be quite different from that of sequential exposure to oxygen then water vapor like Sonnerdorf et al. did. In the present case, as shown in Fig. 10-1 the mixture of water and oxygen did produce substantial amount of hydroxyl species on heavily oxidized Ni surface. In addition it was also observed that the areas of XPS O(1s) high B.E. peaks on Ni(110) were increased even after the entire surface was covered by NiO similar to the result of oxygen-hydrogen exposure. This again suggests that the mixture exposure of either oxygen-water or oxygen-hydrogen is necessary for the formation of (OH) on Ni surface particularly at high oxygen coverage.

Though significant increase of water content (three orders of magnitude higher than "pure" oxygen exposure) occurred for the exposures of water-oxygen mixture as shown in Fig. 10-1 the peak area of adsorbed (OE) on oxygen-water exposed Ni surface is only slightly (~ 25%) larger than "pure" oxygen exposed surface. This indicates that the formation of (OH) is not very sensitive to the partial pressure of water in the UHV (10^{-11} to 10^{-7} Torr). It appears that the amount of (OH) on the surface is determined by some limiting factors like the availability of the sites for the dissociation of (OH).

C. Subsurface Hydrogen

By analogy to surface segregation and chemisorption (145) oxygen may react with the hydrogen from either the vacuum or the

substrate, therefore hydrogen residing in the substrate may also have an effect on the formation of (OH). Askury et al (146) reported that the adsorption of oxygen on a polycrystalline Zr attracts bulk hydrogen forming a hydroxylated surface oxide layer.

In general bulk dissolution of hydrogen does not occur in Ni (147). But the existence of a subsurface hydrogen β_3 state on Ni(110), whose desorption peak was centered at ~435°K in the thermal desorption spectrum, was reported by Harrington et al (148). For an exposure as high as 750 L (0.1 Pa.s) of D_2 during slow cooldown from 520°K to 170°K, the β_3 state saturated only at ~0.06 ML. Though subsurface hydrogen is atomic and expected to be able to react with oxygen readily to form (OH), it is not expected to have significant effects on the formation of (OH) because of its extremely small coverage.

D. Implanted Hydrogen

The O(1s) spectra of both Ar^+ sputtered and sputtered annealed Ni(110) after 300 L of oxygen exposure are compared in Fig 10-2. The high B.E. O(1s) peak on the sputtered surface is twice or large as that on the annealed surface. Norton et al (149) have observed similar results on Ni(100), and they attributed the enhanced high B.E. O(1s) peak solely to defective oxide. As discussed before, no convincing evidence supports the existence of the defective oxide on room temperature oxidized Ni surface. The enhancement of the high B.E. O(1s) peak could be attributed to the reaction of oxygen with

hydrogen implanted during the sputtering process, since a substantial amount of hydrogen, which can serve as an atomic hydrogen reservoir can be retained in the substrate after sputtering.

However, it is expected that implanted hydrogen will be removed by annealing the substrate to a sufficiently high temperature, and consequently a lower amount of (OH) will be formed on the annealed surface as compared to the sputtered one as shown in Fig. 10-2. Based on the attenuated intensity for a homogeneous overlayer,

$$I_{Ni} = I^{\circ}_{Ni} \cdot \exp[-t/(\Omega_{Ni} \sin\theta)] \qquad [10-1]$$

and using the metallic Ni peak areas of both clean and oxidized Ni surfaces, the thickness of "oxide overlayer" on sputtered surface is calculated to be about 1 ML thicker than that on annealed surface. The increased overlayer thickness is attributed to the larger amount of adsorbed (OH) formed on sputtered surface, since the peak areas of O(1s) of Ni oxide are about the same for both sputtered and annealed Ni surfaces.

As reported before, it was also noted that the adsorption of oxygen on Ni can be accelerated by Ar^{+} sputtering. The acceleration has been attributed to the increase of surface defects (54,64). These surface defects may also have effects on the formation of hydroxyl, but it is not possible to separate the effects of surface defect from that of implanted hydrogen in the present study. Possible future work would be to implant deuterium into Ni.

Crystal Orientation Effects

Strong orientation effects have been reported for adsorption of water on Ni surface. Water was found not to be dissociated on either clean or oxygen dosed Ni(111) (151-152), while dissociation of water could be enhanced by the presence of surface oxygen on Ni(110) (137-141). It is worth commenting on the effects of Ni substrate orientation on the formation of (OH) during oxidation.

From the published results (149,151,154), it is found that after oxygen exposures (OH) groups are present on the (100) (110) and (111) as well as the polycrystalline Ni surfaces. The amounts of (OH) on Ni surfaces of different orientations were about equal but slightly larger amount of (OH) on Ni(100) has been reported (149). The strong effect of crystal orientation on adsorption of water was totally not observed in the formation of (OH) on Ni during oxygen exposure again suggesting the mechanism for the formation of (OH) by adsorption of water is different from that by oxygen (oxygen + hydrogen) exposure.

Thermodynamic Factors for (OH) Formation

Results

The XPS O(1s) spectra of Ni NiCr and Cr surfaces after 300 L oxygen exposure at room temperature are compared in Fig.10-3. The O(1s) spectra of Ni and NiCr have two peaks indicating the

formation of both hydroxyl species and oxide on surfaces. While the O(1s) spectrum of oxidized Cr exhibits only one oxide peak, and no hydroxyl species is observed. This is consistent with the previous observation that only one oxidation product Cr_2O_3 is formed on the surface of Cr oxidized in UHV chamber at room temperature (155-157).

Discussion

Calculation of Enthalpy Changes

Thiel and Madey (144) have adopted an analysis which was previously used by Ehrlich (158) for the adsorption of diatomic molecules at metal surfaces. Thiel et al. calculated the enthalpy changes in adsorption and dissociation of water on solid surfaces based upon heats of formation of bulk oxides and hydroxides, but no coverage effects and entropy contributions to free energies were considered in the calculation. The thermodynamic predictions for the water adsorption reactions, like

$$H_2O_{(g)} \rightarrow H_2O_{(a)} \quad \text{(molecular adsorption)}$$

$$H_2O_{(g)} \rightarrow 2\,H_{(a)} + O_{(a)} \quad \text{(complete dissociative adsorption)}$$

and $$H_2O_{(g)} \rightarrow OH_{(a)} + H_{(a)}, \quad \text{(partial dissociative adsorption)}$$

generally agree well with the experimental results. As shown in Fig. 10.4, the enthalpies involved in adsorption and dissociation of

Fig. 10-3 O(1s) spectra at $\theta = 45°$ for polycrystalline pure Ni, pure Cr and NiCr alloy exposed to 300 L O_2

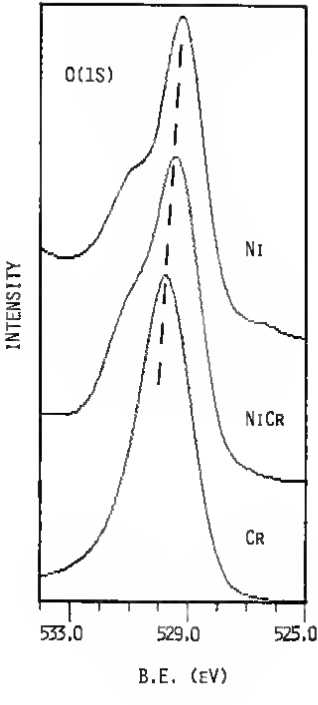
O(1S)
NI
NICR
CR
INTENSITY
533.0
529.0
525.0
B.E. (eV)

Fig 10-4 Enthalpy changes which accompany adsorption and dissociation of water referenced to gas-phase molecular hydrogen and oxygen.

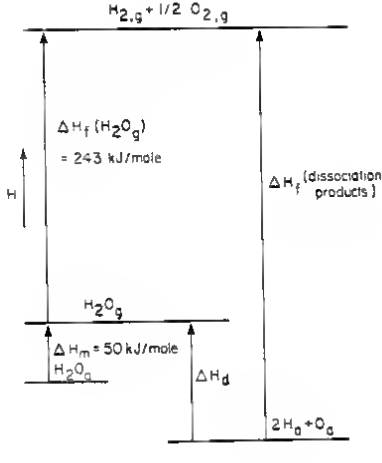
$H_{2,g} + 1/2\ O_{2,g}$
$\Delta H_f (H_2O_g)$
= 243 kJ/mole
H
ΔH_f (dissociation products)
H_2O_g
ΔH_m = 50 kJ/mole
H_2O_a
ΔH_d
$2H_a + O_a$

water are illustrated by using atomic hydrogen and oxygen as dissociated products.

During oxygen exposure several reactions on the metal (Ni, Cr and Fe) surfaces are considered to be relevant to the formation of hydroxyl species and other species. These reactions are

$$H_2O_{(g)} + 1/2\ O_{2(g)} \rightarrow 2\ H_{(a)} + 2\ O_{(a)}, \qquad [10\text{-}2]$$

$$\text{or} \rightarrow 2\ OH_{(a)} \qquad [10\text{-}3]$$

$$H_{2(g)} + 1/2\ O_{2(g)} \rightarrow 2\ H_{(a)} + O_{(a)}, \qquad [10\text{-}4]$$

$$\text{or} \rightarrow OH_{(a)} + H_{(a)}, \qquad [10\text{-}5]$$

$$H_2O_{(g)} \rightarrow 2\ H_{(a)} + O_{(a)}, \qquad [10\text{-}6]$$

$$\text{or} \rightarrow OH_{(a)} + H_{(a)} \qquad [10\text{-}7]$$

The enthalpy changes for reactions [10-2] to [10-7] are calculated following the same treatment of Thiel et al. (14d). As shown in Fig 10-4 all the energies involved in the calculations are referenced to the level of gas-phase molecular hydrogen and oxygen. Because the heat of formation of water is known to be -243 kJ/mole the enthalpy changes for the reactions [10-4] and [10-5] can be obtained by simply adding -243 kJ/mole to those for the reactions [10-6] and [10-7]. The calculated enthalpy changes for the reactions from [10-2] to [10-7] for Ni, Cr and Fe are listed in Table 10-1. For the same reactants the difference in driving forces for producing

$(H_{(a)} + O_{(a)})$ and $OH_{(a)}$, i.e. $(\delta H_2 - \delta H_3)$, $(\delta H_4 - \delta H_5)$ and $(\delta H_6 - \delta H_7)$ are also compared in Table 10-1.

According to the calculated enthalpy changes in Table 10-1 for pure Cr (where $\delta H_2 >> \delta H_3$, $\delta H_4 >> \delta H_5$ and $\delta H_6 >> \delta H_7$), $H_{(a)} + O_{(a)}$ are more thermodynamically favored to form on Cr surface than $OH_{(a)}$. Also because the bonding energy of Cr-O (~383 kJ/mole) is larger than that of Cr-OH (~355 kJ/mole) and Cr-H (~92 kJ/mole), Cr oxide is expected to be the most stable product formed on Cr surface even in the mixture of oxygen and hydrogen (or water) in agreement with the experimental observation.

Based upon the calculated enthalpy changes for Ni in Table 10-1 the driving forces for forming $OH_{(a)}$ are smaller than those for forming $H_{(a)} + O_{(a)}$, and $H_{(a)} + O_{(a)}$ also appear to be more thermodynamically favored to form on the Ni surface than $OH_{(a)}$. In contrast to the case of pure Cr, this thermodynamic prediction does not agree with the experimental observation which shows that both OH and O are present on the oxidized Ni surface.

However as compared to Cr it is found that the difference in the calculated driving forces for forming $(H_{(a)} + O_{(a)})$ and $OH_{(a)}$ on Ni is much smaller. For example, $(\delta H_2 - \delta H_3)$ is only ~70 kJ/mole for Ni while that is ~235 kJ/mole for Cr. The smaller difference in the calculated enthalpy changes probably suggests that Ni exists on the "broadline" i.e. within the limits of the uncertainty of this

Table 10-1 Enthalpy changes (kJ/mole) for reactions [10-2] to [10-7]

	Ni	Cr	Fe
δH_f(M-O), (159)	-260	-383	-272
δH_f(M-M), (159)	-6H	-92	-67
δH_f(M-OH), (159)	-26H	-356	-235
δH_2	-333	-707	-435
δH_3	-253	-669	227
δH_4	-336	-567	-606
δH_5	-296	-668	-302
δH_6	-93	-326	-163
δH_7	-53	-205	-59
$\delta H_2 - \delta H_3$	-80	-238	-212
$\delta H_4 - \delta H_5$	-40	-119	-106
$\delta H_6 - \delta H_7$	-60	-119	-106

crude analysis.*** Furthermore, the small difference in forming ($H_{(a)} + O_{(a)}$) and OH(a) on Ni surface may suggest that the tendencies for forming (OH) and O on Ni surface are close. The bonding energies of Ni-OH and Ni-O are about equal (only 8 kJ/mole in difference) again suggesting that Ni has close affinities to both O and (OH). These analyses are supported by the experimental observation that both hydroxyl and oxide are present on the surface of oxidized Ni

Adsorbed (OH) vs. Hydroxide

Results

The O(1s) and Ni(2p) spectra of Ni(110) after oxygen exposure for 300 L in UHV chamber and after air exposure for 5 minutes are compared in Fig. 10-5. For air-exposed Ni(110) the (OH) component of O(1s) spectra is larger than oxide component and Ni hydroxide is found on the surface. In contrast, for 300 L oxygen-exposed Ni(110) the (OH) component of O(1s) spectra is smaller than oxide component and NiO is the only detectable reaction product for Ni (also see chapter 6). The striking difference suggests that the pressure of reactive gas is important, particularly that of water in the air-exposure case.

*** Similar comment has also been made for the adsorption of water vapor on Ni by Thiel and Madey (144)

Fig. 10-5 O(1s) and Ni($2p_{3/2}$) XPS spectra at θ = 15° for Ni(110) exposed to (a) air for 5 minutes and (b) 300 L O_2.

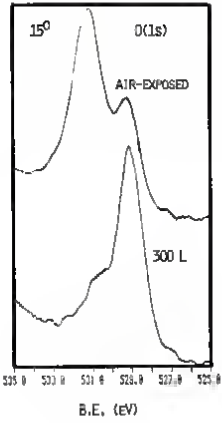
15°
O(1s)
AIR-EXPOSED
300 L
535.0
533.0
531.0
529.0
527.0
525.0
B.E. (EV)
15°
Ni(2P2/3)
AIR-
EXPOSED
300 L
864.0
859.0
854.0
849.0
844.0
B.E. (EV)

Discussion

A. Pure Ni

1. 300 L

Though the affinities of Ni to both O and OH can be close it is found that (OH) is an adsorbed species rather than hydroxide on the 300 L oxidized Ni surface as concluded from chapter 6 and 9. Holloway [160] has suggested that the nucleation of NiO out of chemisorbed oxygen is thermodynamically driven by surface phase transformation which responds to the variable of surface coverage and temperature. Benndorf et al [161] found that NiO nucleates at about 0.66 ML oxygen coverage on Ni(110) at room temperature. By analogy to the nucleation of Ni oxide on Ni surface, Ni hydroxide is expected not to form until a substantial concentration of OH is present on the surface.

It is found that the existence of OH is limited to the first layer of the 300 L oxidized Ni. If the thickness of NiO is assumed to be three monolayers, the coverage of surface OH is estimated to be about 0.3 ± 0.1 ML from the peak areas of hydroxyl and oxide components in the O(1s) spectra using the following equation

$$I_{OH} / I_O = [\theta_{OH} [1-\exp(-1/Q_O \sin\theta)]] / [C_O [1-\exp(-3/Q_O \sin\theta)]] \quad [10-8]$$

where I_i is the peak area for OH or O, θ_{OH} is the coverage of (OH) and C_O is the composition of O in NiO. The coverage of OH is also

estimated to be about 0.1 ML when nucleation of NiO occurs at an oxygen coverage of about 0.6 ML at 20L.

Though the pressure of hydrogen is as high as 59% of that of admitted oxygen, the small coverage of adsorbed OH suggests that the formation of OH is limited by some kinetic factors, such as the sticking coefficients of hydrogen and oxygen. The sticking coefficient of oxygen on clean Ni surface is close to 1, while that of hydrogen is only about 0.2 or less (182). Because both hydroxide and oxide are the competing products during oxygen exposure, and also because the thermodynamic driving forces for hydroxide and oxide can be close (the bond energies of Ni-O and Ni-OH are close), the surface concentrations of OH and O are the key factors to determine which compound to form on surface. For the 300 L oxygen exposure type experiment, since the O/OH ratio is always larger than 6 during the whole course of oxygen exposure, it is not likely for Ni hydroxide to nucleate from such low-density OH at surface.

2 Air Exposure

The major components of atmospheric air are listed in Table 10-2. Water generally is the third most abundant constituent after nitrogen and oxygen, while hydrogen is in minor amount. A relative humidity of 50% at 20°C is equivalent to 8.75 Torr of water. As shown in Fig-10-5, the different oxidation results for air-exposure and 300 L suggest that the pressure of water is important since the

Table 10-2, Components of Atmospheric Air, (from ref (22))

Constituent	Pressure (Torr)
N_2	593
O_2	159
CO_2	0.25
inert gases (Ar + Ne + He + Kr +Xe)	7.1
H_2	0.00038
CH_4	0.0015
N_2O	0.00038
H_2O (at 50% relative humidity and 20°C)	8.8

adsorption or even condensation of water can occur on surface at such large pressure. The large amount of water at surface probably makes the surface reaction much more like bulk solution chemistry or even corrosion. Consequently the amount of (OH) on air-exposed Ni surface is larger (by at least a factor of five) than that on 300 L exposed Ni surface. Following the previous discussion, because the coverage of OH is large on air-exposed Ni surface, Ni hydroxide is expected to form in agreement with the experimental data

5 Ni-Cr Alloy

Unlike pure Ni, Ni hydroxide is formed on NiCr surface even in the UHV condition. It is reasonable to propose that the addition of Cr modifies the mechanism for the formation of OH on NiCr surface. As discussed before, the relative density of OH to O on Ni surface is important for the formation of Ni hydroxide. To assist the formation of Ni hydroxide on NiCr surface, the function of Cr addition must be to increase the density of OH on Ni site.

The preferential oxidation of Cr in NiCr alloy can be quite important for the formation of Ni hydroxide. Because the heat of formation of Cr_2O_3 (756 kJ/mole) is much larger than that of NiO (487 kJ/mole), Cr in NiCr alloy surface may act as a getter site for oxygen and the oxygen initially dissociated at Ni site can be attracted to Cr site to form Cr_2O_3. The strong segregation of Cr as shown in chapter 8 suggests that the mobilities of atoms on NiCr surface can be quite high during oxidation and the mobility of oxygen can be provided by the large heat released by the formation of Cr_2O_3. Compared to Ni, OH is not favored to bond to Cr so that OH can remain at Ni site while O moves to Cr site. As a consequence the OH/O concentration ratio at Ni site can be increased drastically and Ni hydroxide instead of NiO is expected to form.

Another possibility for increasing OH concentration at Ni site is to increase the sticking coefficient or dissociation of hydrogen on Ni by addition of Cr. However, the OH concentration increased is

expected to be small, since the bond energy for Cr-H (-92 kJ/mole) is only slightly larger than that of Ni-H (-48 kJ/mole)

For the oxidation of Ni-based alloys, the effects of the addition of iron are quite similar to addition of chromium. For example, Fe is preferentially oxidized at a lower oxygen exposure than Ni in NiFe alloy [163], and Fe also has stronger affinity to O than OH as compared to Ni (Table 10-1). Oxidation of annealed Ni-24%Fe (100) alloy has been studied by Brundle et al. [163]. From their Ni spectra taken at 13° take-off angle, the reaction product was Ni hydroxide not NiO, similar to the result of NiCr alloy. This suggests that the formation of Ni hydroxide on NiCr is not due to some particular conditions in this study like the high hydrogen pressure or the use of sputtered polycrystalline or (110) face single crystal samples, but rather a universal phenomena among the Ni based alloys with the elements like Cr and Fe

Summary

In summary, four different sources for the formation of (OH) in the UHV condition are investigated. It is found that UHV hydrogen (rather than water) is the major species reacting with oxygen to form (OH) in the present study. Equilibrium subsurface hydrogen is expected to have little effects on formation of (OH), while implanted subsurface hydrogen could contribute substantially on sputtered surface. Difference in the oxidation products on sputtered and

annealed Ni surfaces are attributed to implanted hydrogen.

Hydrogen or water exposure alone does not change the amount of (OH) present on the Ni surface. The exposure of mixtures of oxygen and hydrogen gases is essential to continuous formation (OH) on Ni.

Only Cr oxide is found on the oxidized Cr surface, while both oxide and hydroxyl species are found on the oxidized Ni surface. The enthalpy changes of several reactions regarding the formation of OH, O and H on Ni and Cr surfaces are calculated using heats of formation of bulk hydroxide and oxide. The calculated results are consistent with the experimental data.

It is found that NiO is on the 300 L oxidized Ni surface and Ni hydroxide is on both air-exposed Ni and 300 L oxidized NiCr surfaces. Based on the OH/O concentration ratio, a model is proposed to explain the experimental observation. The addition of Cr to Ni may significantly increase the OH/O ratio in Ni site, and may result in the formation of Ni hydroxide instead of NiO on NiCr surface.

CHAPTER 11
CONCLUSIONS

The studies of oxidation reactions of Ni, Cr and Ni-Cr alloys have led to the following conclusions:

1. Ni segregates preferentially to the surface of atomically clean Ni-Cr alloy. The surface energies per atom of solid Ni and Cr can be used to correctly predict the segregating species.

2. The subsurface region of Ni-Cr alloy is depleted of Ni during Ar^+ bombardment at temperatures above 200°C, which is consistent with the prevailing model of preferential sputtering of Ni caused by the surface segregation of Ni and radiation enhanced diffusion. While the subsurface region of room temperature sputtered Ni-Cr alloy is depleted of Cr. The diffusion rate at room temperature may not be sufficiently large so that surface segregation can't fully occur to deplete Ni. The depletion of Cr probably results from the larger cascade sputtering yield of Cr compared to Ni.

3. Substantial amounts of hydroxyl species are found on both oxidized Ni and oxidized NiCr alloy surfaces. During oxygen exposure in the UHV, hydrogen is the most abundant H-containing residual gas while water is only in minor amount. The hydrogen in UHV system is believed to be the major source for the formation of hydroxyl species on Ni surface. It is found that hydrogen or water exposure alone can not change the amount of (OH) already present on surface. A mixture

exposure of oxygen and hydrogen is essential to the continuous formation of (OH) on Ni surface.

4. Chromium is preferentially oxidized on NiCr alloy surface after 1 to 2 L of oxygen exposure. Reaction of Ni with oxygen occurs more slowly than that of Cr/O_2 reaction, but much more rapidly than for pure Ni. Pure Cr and Cr in Ni-Cr alloy have the same oxidation reaction products, Cr_2O_3. In contrast to Cr, the reaction products for pure Ni and Ni in NiCr alloy are different. After 300 L oxygen exposure, it is found that NiO exists on the pure Ni surface, while Ni hydroxide exists on the Ni-Cr alloy surface.

5. The ESID spectra of 300 L oxidized Ni and NiCr are quite different. Compared to Ni, a large O^+ and a negligibly small $(OH)^+$ are desorbed from oxidized NiCr alloy surface. The magnitudes of the H^+ ESID signals are about the same for both surfaces. These ESID results suggest that the existence of adsorbed surface hydroxyl species on pure Ni, and other types of bonding, for example, H subsurface O bond on NiCr surface.

6. The oxide structure of NiCr alloy after 300 L oxygen exposure in UHV has been studied by ARXPS and ISS. The outer one monolayer oxide is a mixture of Ni hydroxide and Cr oxide, and the inner four monolayers is consisted of Cr oxide, very small amount of NiO and possibly some metallic Ni. In addition, a layer having extra metallic Ni exists in the substrate region next to oxide layer. As compared to the three monolayer NiO formed on pure Ni surface, the formation of Ni hydroxide is limited at first monolayer of oxide.

layer demonstrating the increase of passivation ability of Ni substrate by adding Cr

BIBLIOGRAPHY

1 F P Fehlner "Low-Temperature Oxidation-The Role of Vitreous Oxides" (John Wiley New York, 1986)

2 F P Fehlner and N.F Mott, Oxid of Met 2 59 (1970)

3 D.V Keller Jr , in "Surface and Interface I," edited by J J Burke (Syracuse University Press New York 1967) p 225

4. F.M Fowkes, in "Surface and Interface I " edited by J J Burke (Syracuse University Press New York 1967) p.197

5 D Chandra, T.S Elleman and K Verghese J Nucl Mater 59 263 (1976)

6 R S Timsit, Appl Phys Lett 35 400 (1979)

7 S.M Gondnich M Fathipour, D L Ellsworth and C W Wilmsen J Vac Technol 18 949 (1981)

8. E.H Nicollian and J.R Brews "MOS (Metal-Oxide Semiconductor) Physics and Technology" (John Wiley, New York 1982)

9. M.M Atalla E Tannenbaum and E.J Scheibner, Bell Sys Tech J 38, 749 (1959)

10 O Kubaschewski and B E. Hopkins "Oxidation of Metals and Alloys" (Buttarworth London 1962)

11 C.L Au M A Jacksen and W A Anderson J of Electr Mat 16 301 (1987)

12 G Nocerina and K.E Singer, J Vac Technol 16(2) 147 (1979)

13. S Hofmann and A Zalar, Thin Solid Film 39 219 (1976)

14. K Rieber and L Laasak Thin Solid Film 17 105 (1973)

15 K. Rieber and L Laasak, Thin Solid Film 18 83 (1973).

16. M. Koltai I. Trifonov and H. Czarmann Vacuum, 33 49 (1983)

17. L. Toth, A. Barea, G. Safran, M. Menyhard and T. Koranyi, Vacuum 33, 11 (1983)

18. Metals Handbook, Vol 8, (American Society for Metals, Metals Park, OH 1973), p.291

19. J.J. Quinn and R.B. Elliott, Vacuum 27, 473 (1977)

20. E. Bauer and H. Poppa, Surf. Sci. 99, 341 (1980).

21. C. Benedorf, C. Wohl, M. Ruseckas and F. Thieme, Surf. Sci. 111, 187 (1981)

22. J.F. O'Hanlon, "A User's Guide to Vacuum Technology" (John Wiley, New York, 1980) p.76.

23. T.A. Flaim and P.D. Ownby, J. Vac. Sci. Technol. 8, 661 (197.

24. V.K. Agarwala and T. Fort, Surf. Sci. 45, 470 (1974)

25. P.A. Redhead, J.P. Hobson and E.V. Kornelsen, "The Physical Basis of Ultrahigh Vacuum" (Chapman and Hall, London, 1968) p.419,

26. W.N. Riggs and M.J. Parker in "Methods of Surface Analysis," edited by A.W. Czanderna (Elsevier, Netherlands, 1975) p.103-157

27. D.S. Briggs and M.P. Seah, "Practical Surface Analysis by Auger and X-ray Photoelectron Spectroscopy" (Wiley, Chichester, U.K. 1983).

28. H. Iwasaki, K. Nishitani and S. Nakamura, Jpn. J. Appl. Phys. 17, 1519 (1978)

29. C.S. Fadley, "Progress in Surface Science," edited by S.G. Davison (Pergamon, New York, 1985) p.12

30. W.F. Engelhoff, J. Vac. Sci. Technol. A3, 1511 (1985)

31. T.M. Buck in 'Methods of Surface Analysis,' edited by A.W. Czanderna (Elsevier, Netherlands, 1975). p.75-100

32. J.A. Van den Berg and D.G. Armour, Vacuum 31, 259 (1981).

33. M.L. Knotek, Phys. Today Sept., 24 (1984)

34. T.E. Madey and R. Stockbauer, in "Methods of Experiemtal Surface Science," edited by R.L. Park and M.G. Lagally (Academic Press, New York, 1985)

35 G S. Hoflund, Scan. Elec. Micro. 4 1391 (1985).

36 F F. Abraham and C.R. Brundle, J. Vac. Sci. Technol. 18 506 (1981).

37. A.R. Miedema, Philips Tech. Rev. 36 217 (1976).

38. S.P. Frankenthal and S.J. Siconolfi, Surf. Sci. 119 331 (1982).

39. L.E. Murr, 'Interfacial Phenomena in Metals and Alloys' (Addison-Wesley Reading, MA, 1975).

40 R.S. Polizzotti and J.J. Burton, J. Vac. Technol. 14, 347 (1977).

41 V.K. Kumikov and Kh B. Khokonov, J. Appl. Phys. 54 1346 (1983).

42 D.G. Swartzfager, S.S. Ziemecki and M.J. Kelley, J. Vac. Technol. 19(2) 185 (1981).

43 R. Kelly, Surf. and Interf. Anal. 7,1, 1 (1985).

44 T.D. Buesing, P.M. Holloway, Y.X. Wang, J.F. Moulder and J.S. Hammond, to be published in J. Vac. Technol.

45. H. Wiedersich, Nucl. Instru. Meth. in Phys. Res. B7/8, 1 (1985).

46 P.S. Ho, Surf. Sci. 72, 253 (1978).

47. T.D. Buesing and P.M. Holloway, J. Vac. Technol., A3(5) 1973 (1985).

48. P. Sigmund, in "Sputtering by Particle Bombardment I," Topics Appl. Phys., Vol.47, edited by R. Behrisch (Springer-Verlag, Berlin, 1981).

49. J.S. Malherbe, S. Hofmann and J.M. Sanz, to be published in Surface Science.

50. J.C. Pivin, J. Mater. Sci. 18. 1267 (1983).

51. B. Kelly, Surf. Sci. 100, 85 (1980).

52. P. Wynblatt and R.C. Ku, in 'Interface Segregation' edited by W.C. Johnson and J.M. Blakely (American Society for Metals, Metal Park, OH, 1979). p 133.

53 R Hultgren, P D Desai, D T Hawkins, M Gleiser, K K Kelley and D D Wagman, "Selected Values of Thermodynamic Properties of the Elements" (ASM Cleveland, OH 1973)

54 P B Holloway, J Vac. Sci. Technol 18(2) 653 (1981)

55 P B Holloway and J M Buddenn, Surf Sci 43, 123 (1974)

56. P.B. Holloway and J.B. Huddens, Surf. Sci. 42, 141 (1974).

57. C. Palacio, B.J. Mathieu and D. Landolt, Surf. Sci. 182, 41 (1987).

58. J.S. Foord and R.M. Lambert, Surf. Sci, 181, 513 (1985)

59. G. Gewinner, J.C. Peruchetti and A. Jaegle, Surf. Sci. 78, 479 (1978).

80. M.W. Roberts and C.S. McKee, Chemistry of the Metal-Gas Interface (Clarendon, Oxford, 1978), p 442.

81. C.R. Brundle and A.F. Carley, Chem. Phys. Let. 11, 423 (1975).

82 K Wandelt, Surf. Sci Rep 2, (1982)

83 P.A. Thiel and T.E. Madey Surf Sci Rep, 7, Nos 6-8, (1987)

84. C.R. Brundle and J.Q. Broughton, "The Chemical Physics of Solid Surfaces and Heterogeneous Catalysis ' Vol 3B, edited by D A King and D P Woodruff (Elsevier, Amsterdam to be published)

85 G Gewinner, J C Peruchetti, A Jaegle and A. Malt, Surf Sci 78 439 (1978)

86 J S Foord and R M Lambert, Surf. Sci 71, 513 (1985)

87 C. Palacio, B.J. Mathieu and D. Landolt, Surf. Sci. 182, 41 (1987).

88. P R. Norton, R.L. Tapping and J.W. Goodale, Surf. Sci. 65, 13 (1977).

89. B S Kim and B Winograd, Surf Sci 41 825 (1974).

70 N G. Krishnan, W.N. Delgass and W.D. Robertson, Surf. Sci 57, 1 (1976).

71. S. Evans, J Pielaszek and J M Thomas Surf Sci 55, 844 (1976)

72. T. Fleisch, N. Winograd and W.N. Delgass, Surf. Sci. 78, 144 (1978).

73. M.W. Roberts and S. St. C. Smart, Surf. Sci. 100, 590 (1980).

74. S.J. Behm and C.R. Brundle, J. Vac. Sci. Technol. A1(2), 1223 (1983).

75. H. Sopster and C.R. Brundle, J. Vac. Sci. Technol. 16(2), 548 (1979).

76. H. Sopster and C.R. Brundle, La Vide 201, 275 (1981).

77. P.M. Holloway and R.A. Outlaw, Surf. Sci. 111, 300 (1981).

78. J.R. McKay and V.E. Seatich, Phys. Rev. B32, 6764 (1985).

79. R.L. Knotek, V.O. Jones and V. Sehn, Phys. Rev. Lett. 43, 330 (1977).

80. M.L. Knotek, Surf. Sci. 91, L17 (1980).

81. M.L. Knotek, Surf. Sci. 101, 334 (1980).

82. C.R. Brundle, E. Silverman and R.J. Madix, J. Vac. Sci. Technol. 16(3), 474 (1979).

83. C.P. Li, R. Proctor and P.M. Batcules, Appl. Spectrosc. 38, 880 (1984).

84. G.K. Wertheim and P.A. Citrin, in 'Photoemission in Solids II' edited by M. Cardona and L. Ley (Springer-Verlag, New York 1979) p 197.

85. G.A. Vernon, G. Stucky and T.A. Carlson, Inorg. Chem. 15, 278 (1976).

86. M. Screcce, J. Electron Spectrosc. Relat. Phenom. 15, 311 (1980).

87. S. Doniach and M. Sunjic, J. Phys. C3, 285 (1970).

88. G.D. Mahan, Phys. Rev. B. 11, 4814 (1975).

89. E. Taglauer and W. Heiland, Appl. Phys. 9, 261 (1976).

90. B.M. Bromgerema, R.J. Sparnaay and T.M. Buck, Surf. Sci. 71, 657 (1978).

91 T M Buck in "Methods of Surface Analysis," edited by A W Czanderna, (Elsevier, Netherlands 1975) p 86

92 M P Seah Surf Interface Anal 9, 85 (1987)

93 M P Seah, Surf. Interface Anal. 9, 85 (1987)

94 J M Sanz and S Hofmann Surf Interface Anal. 8, 147 (1986)

95, C S Fadley, "Progress in Surface Science," edited by S G Davison (Pergamon, New York, 1985)

96 C.S Fadley, Prog Solid State Chem. 11, 265 (1976)

97 C Palacin H J Mathieu and D Landolt, Surf Sci 182 41 (1987)

98, M.L Knotek, Phys Today Sept 24 (1984)

99 T.E Madey and R Stockbauer, in "Methods of Experimental Surface Science," edited by E L Park and D G Lagally (Academic Press, New York 1985)

100 G.S Goflund, Scan. Elec. Micro. IV 1391 (1985)

101 G.R Floyd and R.B Prince, Surf. Sci. 59, 631 (1976).

102 M.L Knotek and P.J Feibelman, Phys Rev Lett 40 964 (1978)

103 D Beezel and R Gomer, J. Chem. Phys 41, 3329 (1964)

104 P.A Redhead J Phys 42 886 (1964)

105 B.B Baddeo, J. Vac. Sci. Technol. 13 228 (1976)

106 G Biehne and B Loach, Surf. Sci. 111, 344 (1981)

107 B.C Gerritsen, B.P Bruijn, J. Verheoven and M J Van Der Wiel, Surf. Sci 139, 16 (1984)

108 J. Verheoven, M.H Dang and J J Czyzewski, Surf. Sci. 143, 31 (1984)

109 B B. Band and J Verheoven, Surf Sci. 175, 325 (1986)

110. P W Dawson and M.L deBoer Surf Sci 122 588 (1982)

111 E. Bertel R Stockbauer S L Burtz D A Banaker and T E. Madey Phys Rev B31 5580 (1985)

112 E. Bertel, R. Stockbauer, R.L. Kurtz, T.E. Madey and D.A. Knauer, Surf. Sci. 152/153, 776 (1985).

113 N.D. Shinn and T.E. Madey, Phys. Rev. Lett. 53, 2481 (1984)

114. N.D. Shinn and T.E. Madey, Phys. Rev. B33, 1464 (1986).

115 N.D. Shinn and T.E. Madey, Surf. Sci. 173, 379 (1986).

116 N.D. Shinn and T.E. Madey, Surf. Sci. 176, 635 (1986).

117 N.D. Shinn and T.E. Madey, Nucl. Instru. Meth. in Phys. Res. B13, 537 (1986).

118 T.E. Madey, Surf. Sci., 94, 483 (1980)

119 M.L. Knotek, V.O. Jones and V. Rehn, Phys. Rev. Lett. 43, 300 (1977).

120 M.L. Knotek, Surf. Sci. 91, L17 (1980).

121 M.L. Knotek, Surf. Sci. 101, 334 (1980).

122 W. Gopel, G. Rocker and R. Feierabend, Phys. Rev. B. 28, 3427 (1983).

123 F.P. Netzer and T.E. Madey, Phys. Rev. Lett. 47, 928 (1981).

124 T.E. Madey and F.P. Netzer, Surf. Sci. 117, 549 (1982).

125 C. Benndorf, C. Nobl and T.E. Madey, Surf. Sci. 138, 292 (1984).

126 C. Benndorf and T.E. Madey, Surf. Sci. in press

127 E. Bauer and H. Poppa, Surf. Sci. 99, 341 (1980)

128 P.A. Thiel and T.E. Madey, Surf. Sci. Rep. 7, Nos. 6-8 (1987)

129 D. Litchman, Surf. Sci. 90, 579 (1979).

130 A. Bannigbeyer, P. Bockmann, K.H. Muller and M. Schenmer, Surf. Sci. 89, 701 (1979).

131 M.Y. Wang, F. Ohuchi and P.H. Holloway, J. Vac. Sci. Technol. A2, 732 (1984).

132 S. Andersson and J.W. Davenport, Solid State Commun. 28, 677 (1978).

133 L.M. Moroney, R.C. Smart and M.W. Roberts, J. Chem. Soc., Faraday Trans 79, 1769 (1983).

134 S. Bourgeois and M. Perdereau. Surf. Sci. 117, 165 (1982).

135 S Bourgeois and M Perdereau, J Microsc Spectrosc. Electron 6, 565 (1981).

136 A Benninghoven, F. Beckmann, K.M. Muller and M. Schemmer. Surf. Sci. 89, 701 (1979).

137. C. Brandorf, C. Nobl, M. Buseneberg and F. Thieme, Surf. Sci. 111, 87 (1981).

138 C. Brandorf, C. Nobl and F Thieme. Surf. Sci. 121, 249 (1982).

139 C Brandorf, C Nobl and T Madey, Surf. Sci 138, 292 (1984)

140. M. Mock, U. Selp, I. Busenghanm, K. Wandelmann and J. Kuppers Surf. Sci 177, L978 (1986)

141. C. Brandorf and T. Madey, Surf. Sci , in press.

142 J.M. McKay and V.E. Henrich J. Vac. Technol A5(4) 722 (1987).

143 J.M. McKay and V.E. Henrich Phys. Rev. B32 5764 (1985)

144 P.A. Thiel and T.E. Madey, Surf. Sci. Rep. 7, Nos. 6-8 (1987).

145 J.M. Blakely and J.C. Shelton in "Surface Physics of Materials" Vol 1 edited by J.M. Blackely (Academic Press New York 1977) p 189 - 239.

146 D.A. Asbury, G.B. Hoflund, W.J. Patterson, R.E. Gilbert and R.A. Outlaw Surf. Sci. 185, 213 (1987).

147 T.E. Jackman, K. Griffiths, W.N. Unertl, J.A. Davie, K.H. Gurtler, D.A. Barrington and P.R. Norton. Surf. Sci. 179, 297 (1987).

148 D.A. Barrington and P.R. Norton. Surf. Sci. in press.

149 P.R. Norton, R.L. Tapping and J.B. Goodale, Surf. Sci. 65, 13 (1977)

150 T.E. Madey and F.P. Netzer, Surf. Sci. 117, 549 (1982).

151. C. Nobl and C. Brandorf, Surf. Sci. 182, 499 (1987).

152. C. Benndorf and C. Nobl, J. Vac. Technol. 15(4), 696 (1978).

153. S. Sapotar and C.R. Brundle, J. Vac. Technol. 16(2), 548 (1979).

154. M.G. Krishnan, W.N. Delgass and W.D. Robertson, Surf. Sci. 57, 1 (1976).

155. C. Palacio, M.J. Mathieu and D. Landolt, Surf. Sci. 182, 41 (1987).

156. J.S. Foord and R.M. Lambert, Surf. Sci. 161, 513 (1985).

157. G. Gewinner, J.C. Peruchetti and A. Jaegle, Surf. Sci. 78, 479 (1978).

158. J.B. Benziger, Appl. Surf. Sci. 6, 105 (1980).

159. D.D. Wagman, W.H. Evans, V.B. Parker, R.H. Schumm, I. Halow, S.M. Bailey, K.L. Churney and R.L. Nuttall, J. Phys. Chem. Ref. Data, Suppl. 2 (1982).

160. P.W. Palmberg, J. Vac. Technol. 18(2), 653 (1981).

161. C. Benndorf, B. Egert, C. Nobl, B. Seidel and F. Thieme, Surf. Sci. 92, 636 (1980).

162. K.D. Rendulic and A. Winkler, Surf. Sci. 74, 318 (1978).

163. C.R. Brundle, E. Silverman and M.J. Madix, J. Vac. Sci. Technol. 16(2), 474 (1979).

BIOGRAPHICAL SKETCH

Shin-Puu Jeng was born in Taipei, Taiwan, Republic of China, on January 16, 1957. In June 1979, he received his B.S. in materials science and engineering from the National Tsing-Hua University in Taiwan. After two years of required military service, he worked as an assistant engineer for the Precision Instrument Development Center of the National Science Council in Taiwan for one year. He went to the United States in August 1982 and received his M.S. in materials science from the State University of New York at Stony Brook in April, 1984. He then entered the University of Florida and has pursued the degree of Doctor of Philosophy since then.

His research interests include gas/solid interaction and physical and chemical properties of thin film and interfacial region of solids. He has extensive experience in various surface analytical techniques, including AES, ESCA, ISS, SIMS and ESID. He is a member of the American Vacuum Society, the Materials Research Society, Tau Beta Pi honorary and Alpha Sigma Mu honorary.

Shin-Puu Jeng married the former Shirling Pan on September 3, 1981, and they have a son, Thomas, born in Gainesville, Florida, on September 3, 1986.

I certify that I have read this study and that in my opinion it conforms to acceptable standards of scholarly presentation and is fully adequate, in scope and quality, as a dissertation for the degree of Doctor of Philosophy.

Paul H. Holloway, Chairman
Professor of Materials Science
and Engineering

I certify that I have read this study and that in my opinion it conforms to acceptable standards of scholarly presentation and is fully adequate, in scope and quality, as a dissertation for the degree of Doctor of Philosophy.

Christopher Patrick
Associate Professor of Materials
Science and Engineering

I certify that I have read this study and that in my opinion it conforms to acceptable standards of scholarly presentation and is fully adequate, in scope and quality, as a dissertation for the degree of Doctor of Philosophy.

Robert T. DeHoff
Professor of Materials Science
and Engineering

I certify that I have read this study and that in my opinion it conforms to acceptable standards of scholarly presentation and is fully adequate, in scope and quality as a dissertation for the degree of Doctor of Philosophy.

E. Dow Whitney
Professor of Materials Science and Engineering

I certify that I have read this study and that in my opinion it conforms to acceptable standards of scholarly presentation and is fully adequate, in scope and quality as a dissertation for the degree of Doctor of Philosophy.

Gar B. Hoflund
Professor of Chemical Engineering

This dissertation was submitted to the Graduate Faculty of the College of Engineering and to the Graduate School and was accepted as partial fulfillment of the requirements for the degree of Doctor of Philosophy.

April, 1988

Dean, College of Engineering

Dean, Graduate School